Supplementary for the manuscript "Weakening Correlation and Delaying Response Time of Ecosystem Water Use Efficiency to Drought"

Zijun Wang[a], Rong Wu[b], Yangyang Liu[c,*], Zhaoying Zhang[d], Zhongming Wen[c], Zhenqian Wang[e], Stephen Sitch[f], Wenping Yuan[g]

[a] *College of Water Resources and Architectural Engineering, Northwest A&F University, Yangling, Shaanxi 712100, China*

[b] *Shenzhen Key Laboratory of Precision Measurement and Early Warning Technology for Urban Environmental Health Risks, School of Environmental Science and Engineering, Southern University of Science and Technology, Shenzhen 518055, China*

[c] *College of Grassland Agriculture, Northwest A&F University, Yangling, Shaanxi 712100, China*

[d] *Jiangsu Center for Collaborative Innovation in Geographical Information Resource Development and Application, International Institute for Earth System Sciences, Nanjing University, Nanjing, Jiangsu 210023, China*

[e] *Department of Physical Geography and Bolin Centre for Climate Research, Stockholm University, Stockholm 10691, Sweden*

[f] *Faculty of Environment, Science and Economy, University of Exeter, Exeter, UK*

[g] *Institute of Carbon Neutrality, Sino-French Institute for Earth System Science, College of Urban and Environmental Sciences, Peking University, Beijing, China*

* *Corresponding Author. Yangyang Liu (*lyywylnwafu@163.com*).*

Post address: College of Grassland Agriculture, Northwest A&F University, Xinong Road 22, Yangling 712100, China.

The supplementary includes the following contents:

1. Figure S1. Global distribution of the 85 selected FLUXNET 2015 sites.
2. Figure S2. Site-scale validation of WUE derived from multi-source remote sensing data against WUE calculated from the 85 FLUXNET 2015 sites.
3. Figure S3. Spatial distribution of vegetation types.
4. Figure S4. Spatial distribution of the drought gradient.
5. Figure S5. Temporal trends in the R_{max} and T_{opt} between global WUE and SPEI under (a) a 16-year and (b) a 20-year moving window.
6. Figure S6. Performance validation of remotely sensed WUE against seven TRENDY models and the multi-model ensemble mean.
7. Figure S7. Temporal trends in the R_{max} between WUE and SPEI derived from various TRENDY models under 16-year, 18-year, and 20-year moving windows.
8. Figure S8. Temporal trends in the T_{opt} between WUE and SPEI derived from various TRENDY models under 16-year, 18-year, and 20-year moving windows.
9. Figure S9. Spatiotemporal variations in (1) R_{max} and (2) T_{opt} between WUE and SPEI (1) derived from various TRENDY models under a 16-year moving window.
10. Figure S10. Spatiotemporal variations in (1) R_{max} and (2) T_{opt} between WUE and SPEI (1) derived from various TRENDY models under a 18-year moving window.
11. Figure S11. Spatiotemporal variations in (1) R_{max} and (2) T_{opt} between WUE and SPEI (1) derived from various TRENDY models under a 20-year moving window.
12. Figure S12. Variable contributions of CO_2, CLI, and LCC to R_{max} and T_{opt} under a 16-year moving window. (The left and right columns represent contributions to correlation coefficients and lag times, respectively, while the rows from top to bottom indicate the contributions of CO_2, CLI, and LCC.)

Supplementary Materials

Supplementary Figures

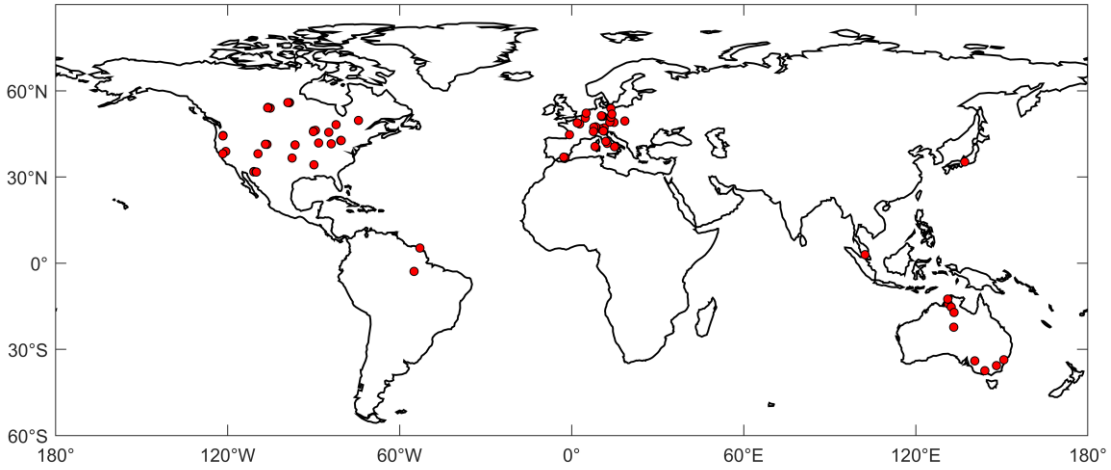

Figure S1. Global distribution of the 85 selected FLUXNET 2015 sites.

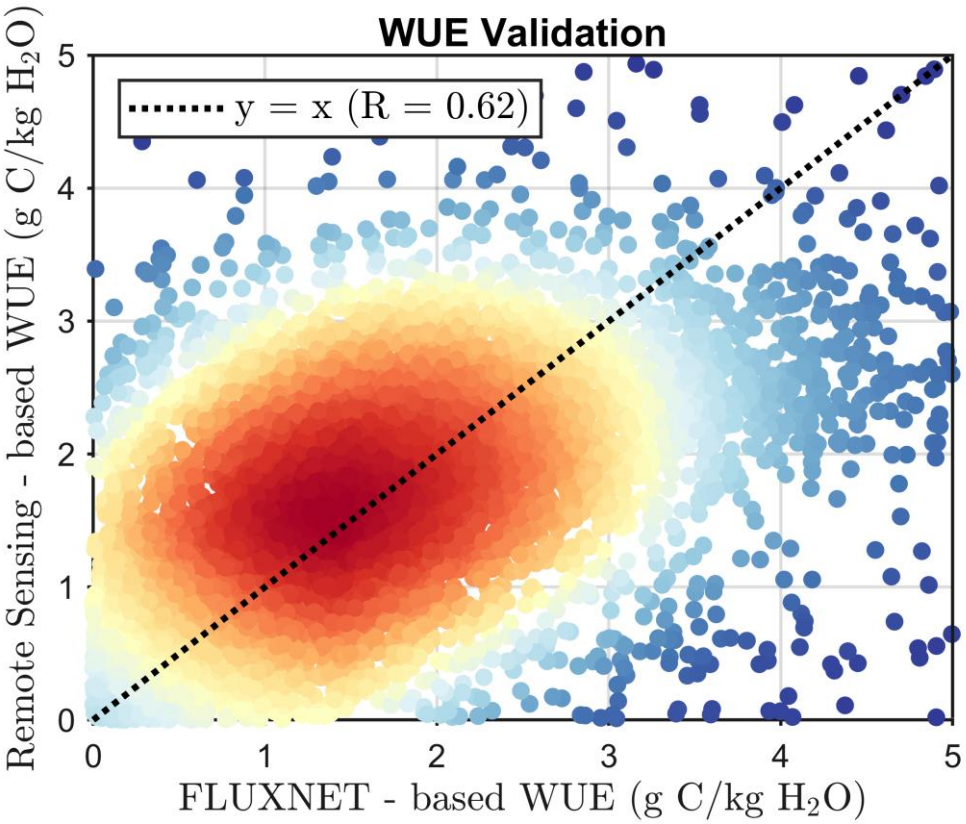

92

93 Figure S2. Site-scale validation of WUE derived from multi-source remote sensing

94 data against WUE calculated from the 85 FLUXNET 2015 sites.

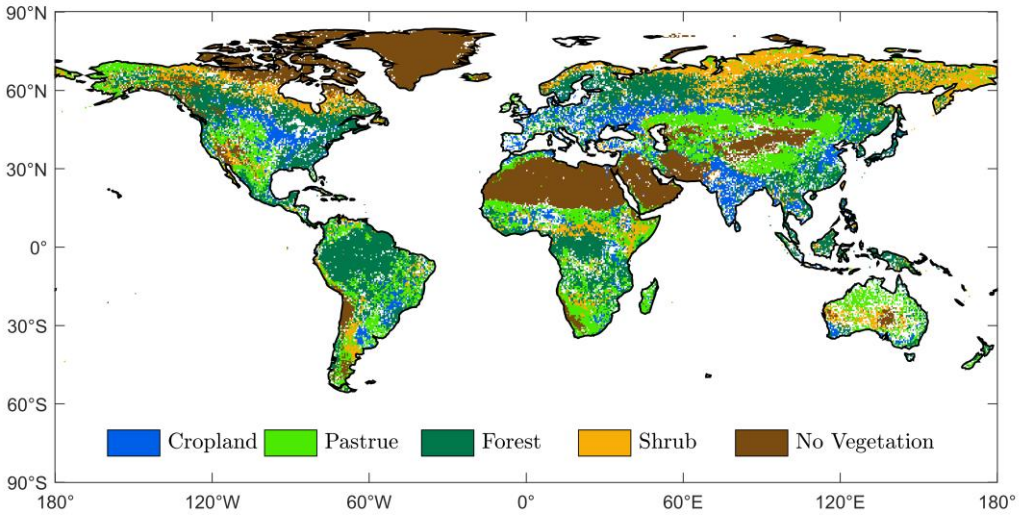

Figure S3. Spatial distribution of vegetation types.

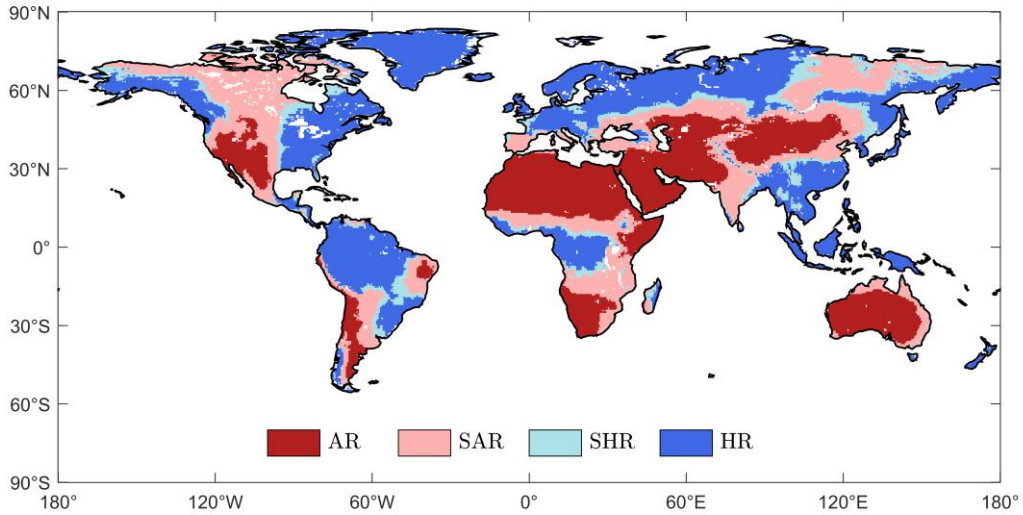

Figure S4. Spatial distribution of the drought gradient.

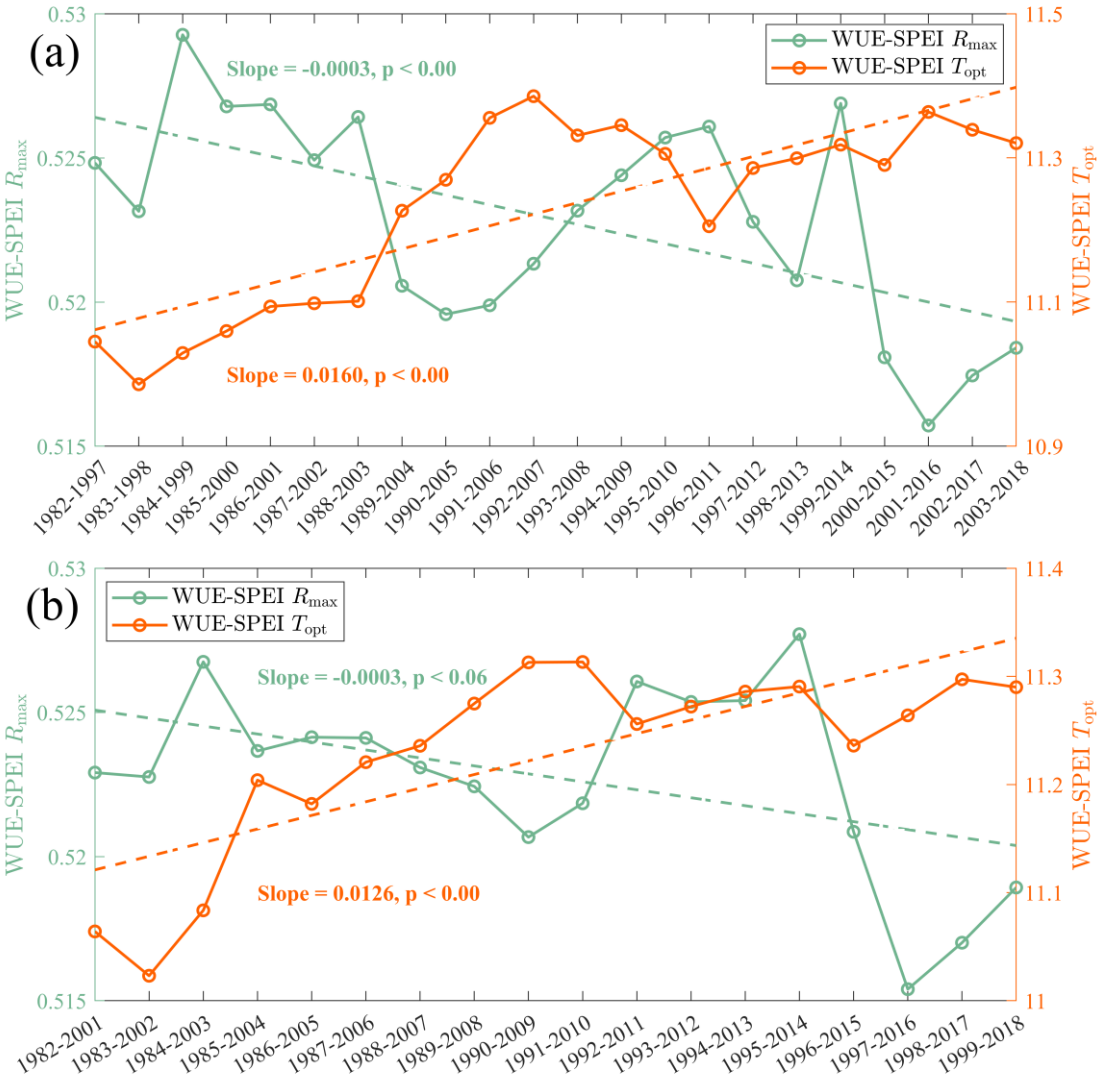

Figure S5. Temporal trends in the R_{max} and T_{opt} between global WUE and SPEI under (a) a 16-year and (b) a 20-year moving window.

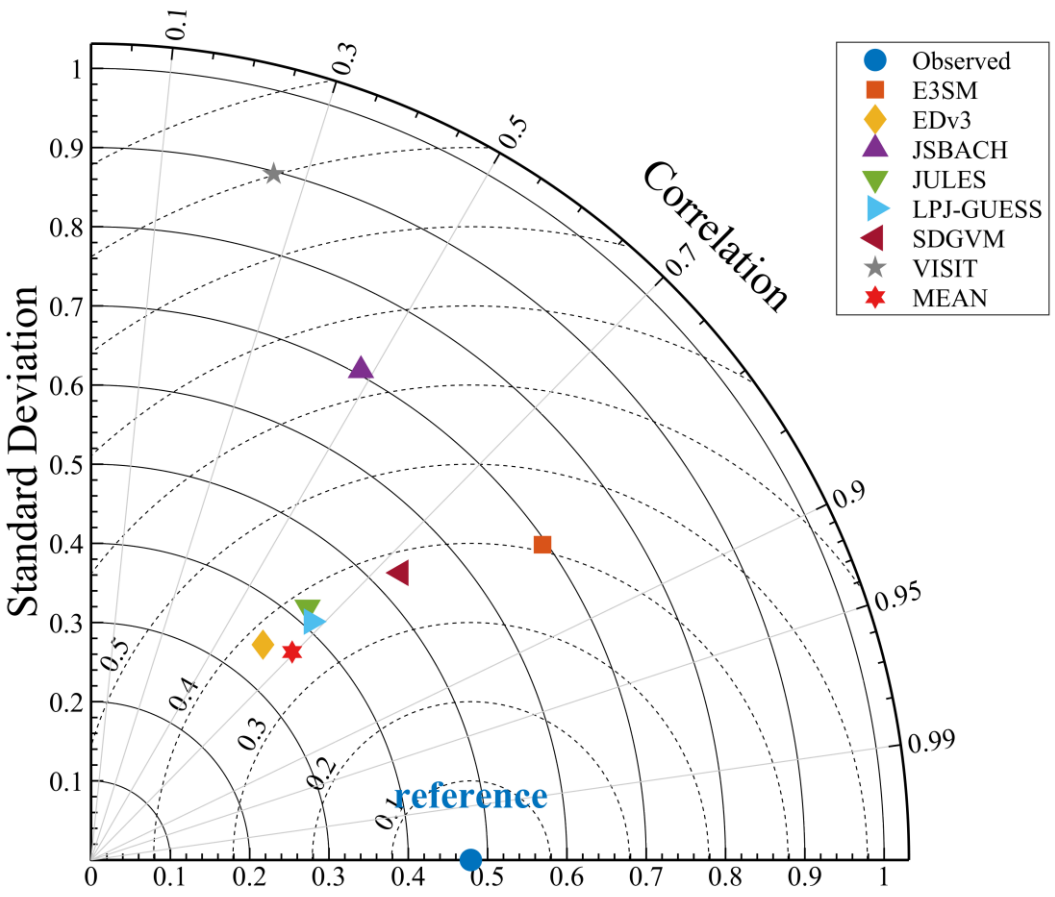

Figure S6. Performance validation of remotely sensed WUE against seven TRENDY models and the multi-model ensemble mean.

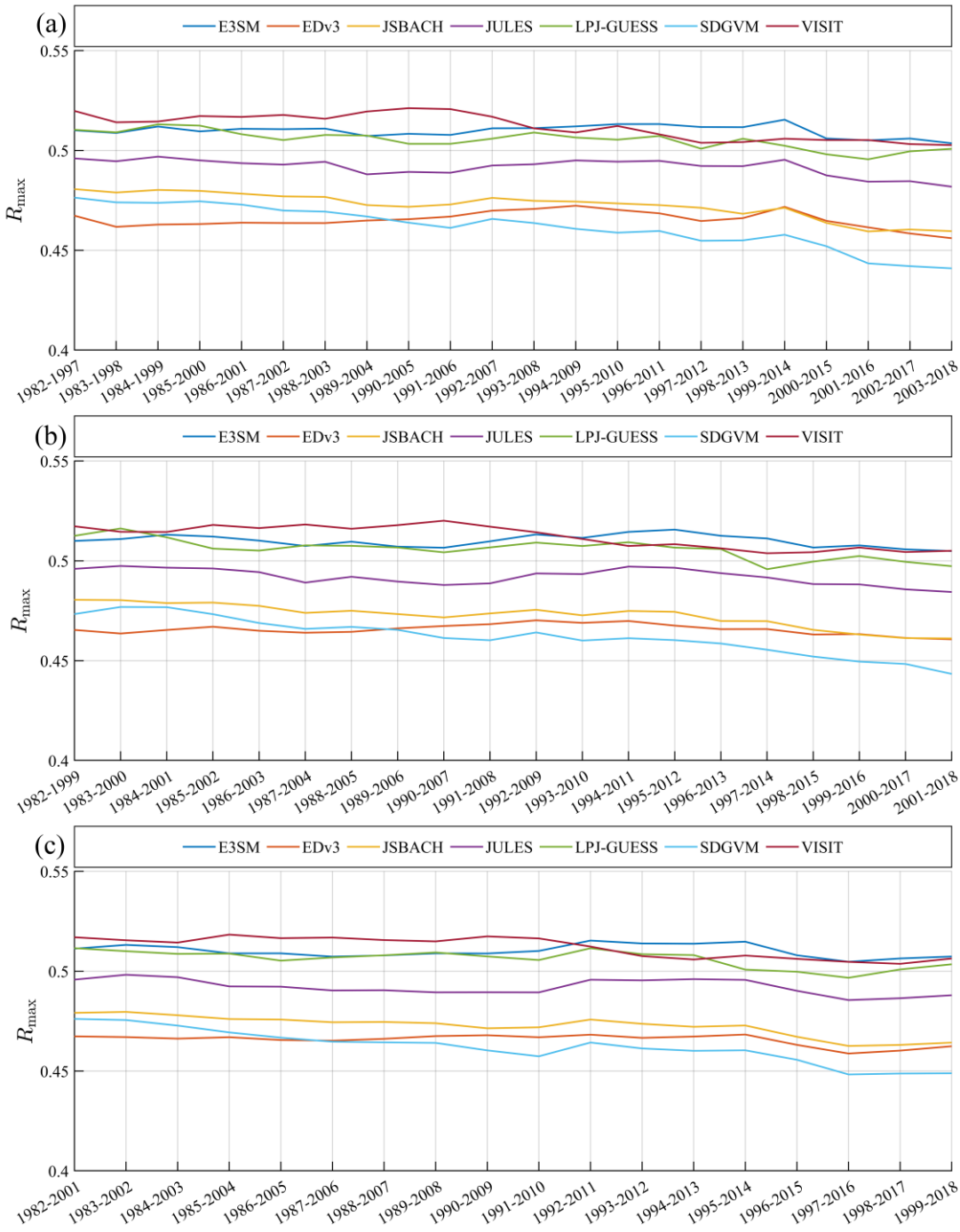

Figure S7. Temporal trends in the R_{max} between WUE and SPEI derived from various TRENDY models under 16-year, 18-year, and 20-year moving windows.

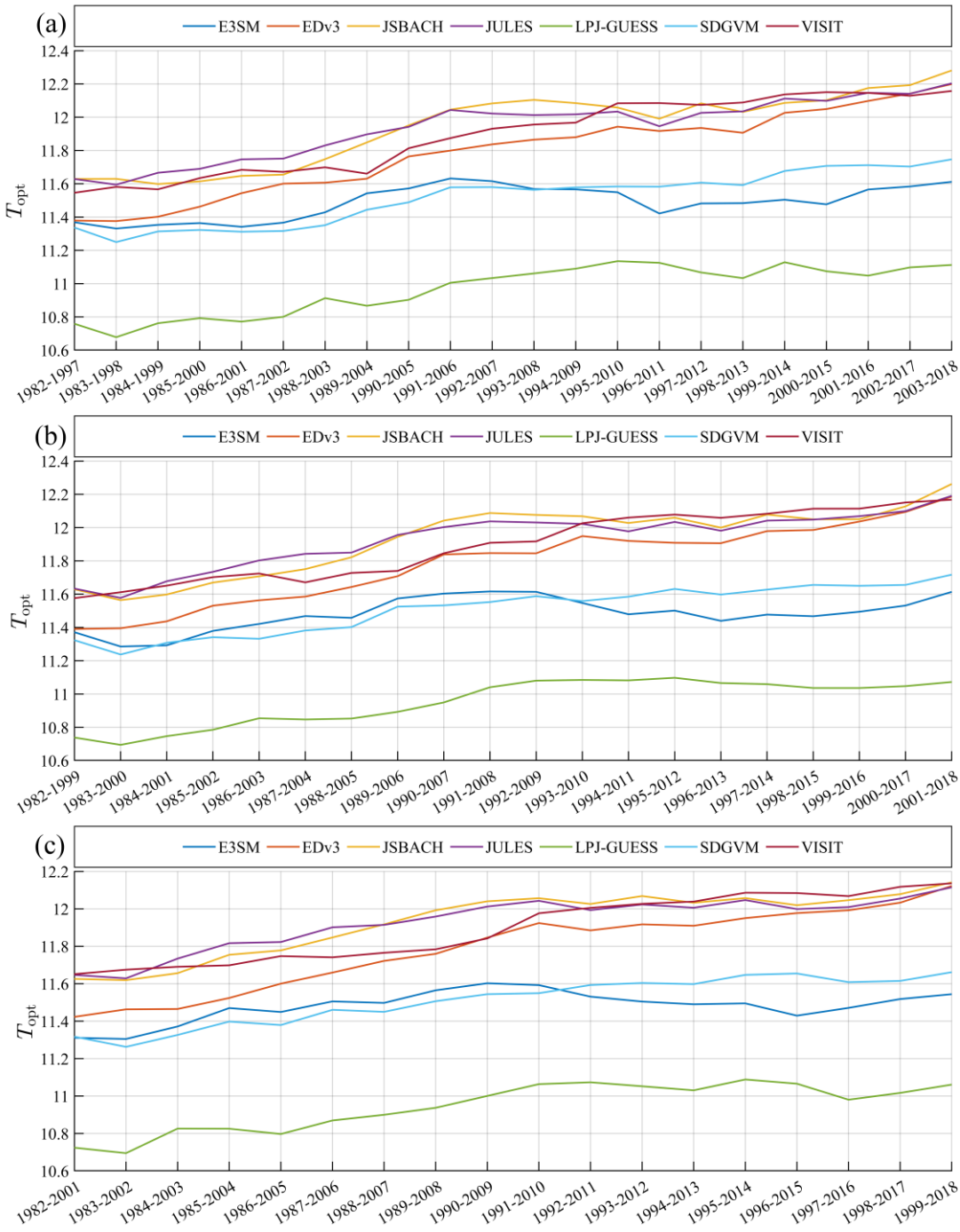

Figure S8. Temporal trends in the T_{opt} between WUE and SPEI derived from various TRENDY models under 16-year, 18-year, and 20-year moving windows.

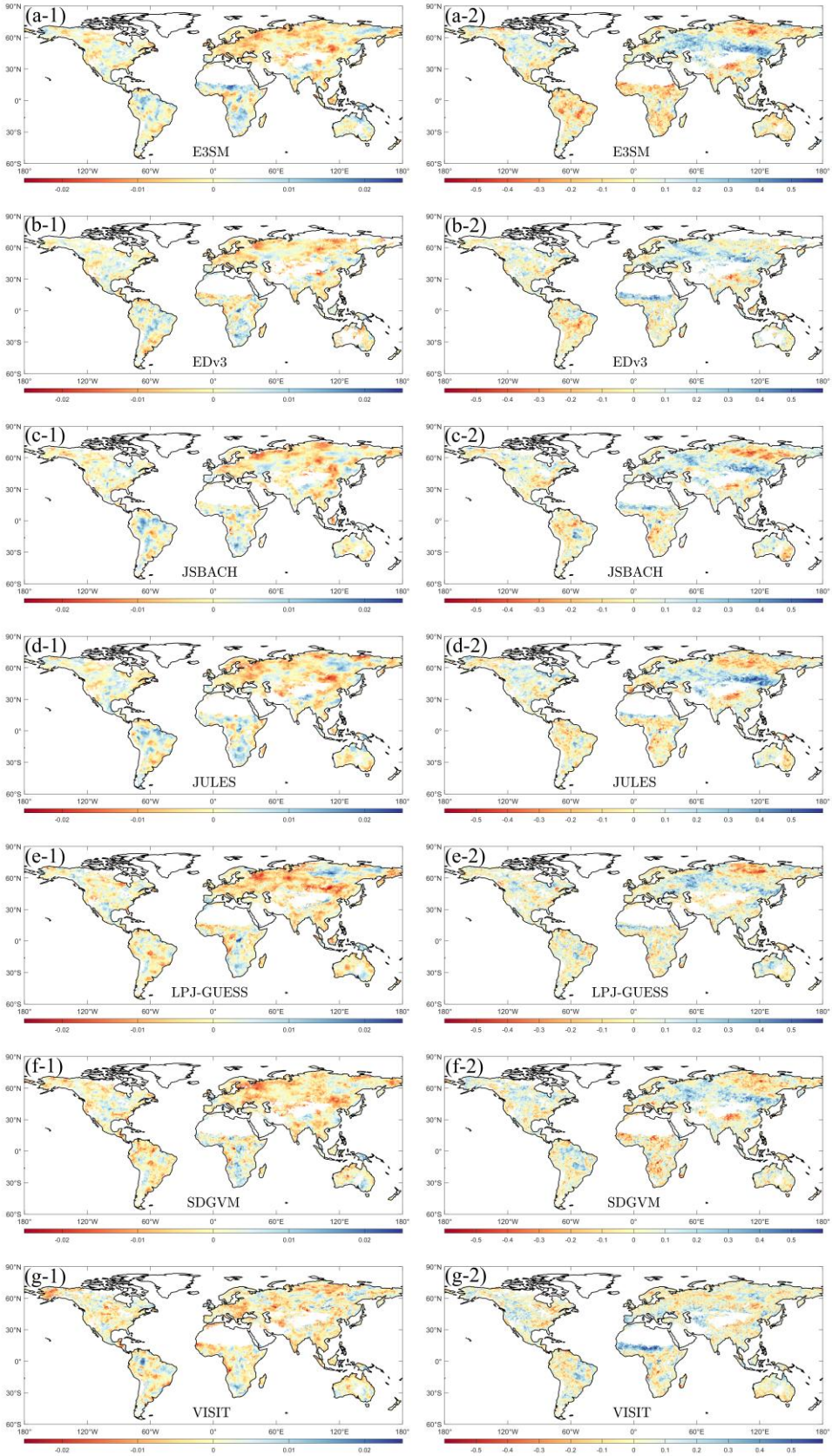

112

113 Figure S9. Spatiotemporal variations in (1) R_{max} and (2) T_{opt} between WUE and

114 SPEI (1) derived from various TRENDY models under a 16-year moving window.

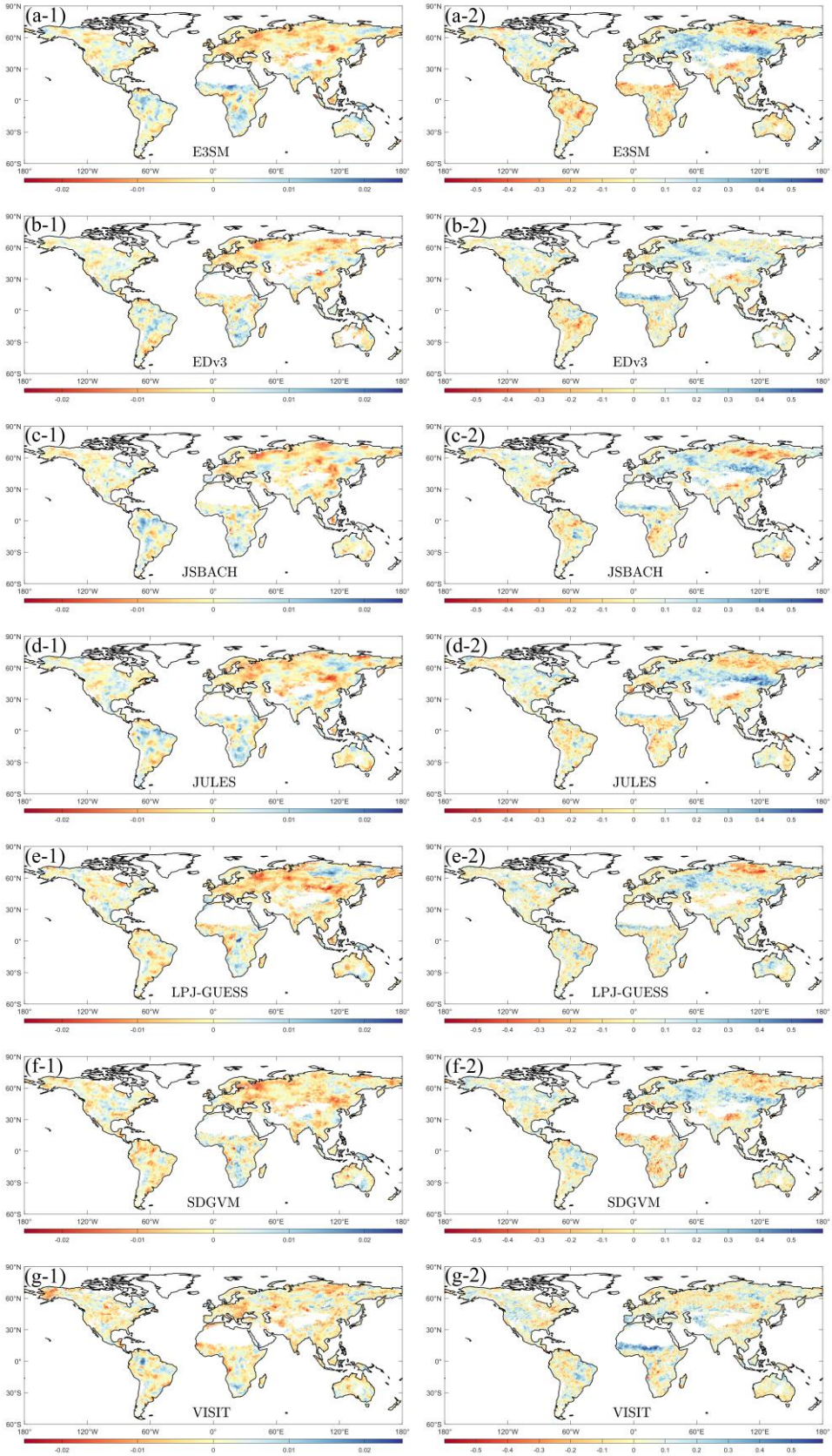

115

116 Figure S10. Spatiotemporal variations in (1) R_{max} and (2) T_{opt} between WUE and

117 SPEI (1) derived from various TRENDY models under a 18-year moving window.

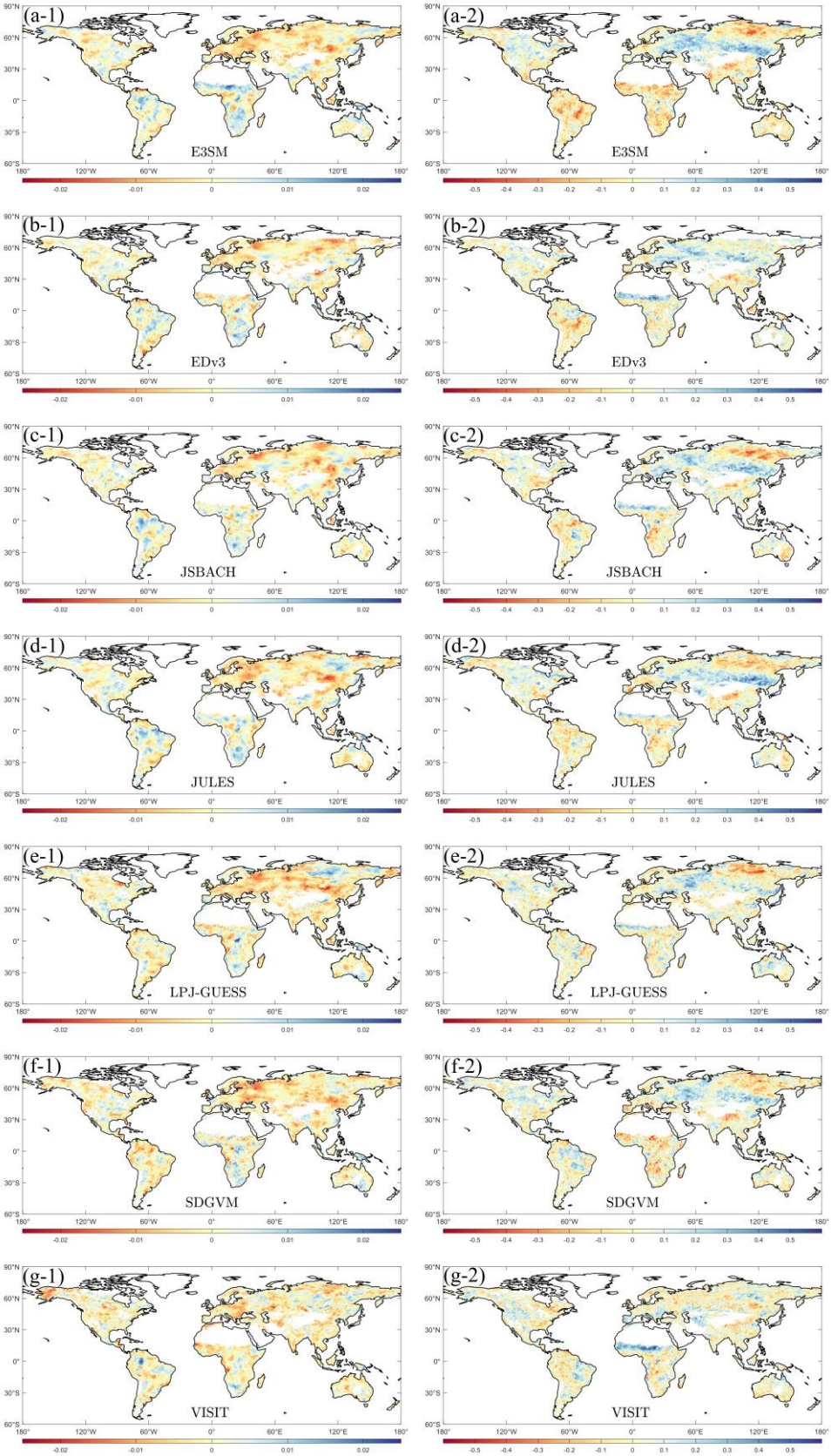

118

119 Figure S11. Spatiotemporal variations in (1) R_{max} and (2) T_{opt} between WUE and

120 SPEI (1) derived from various TRENDY models under a 20-year moving window.

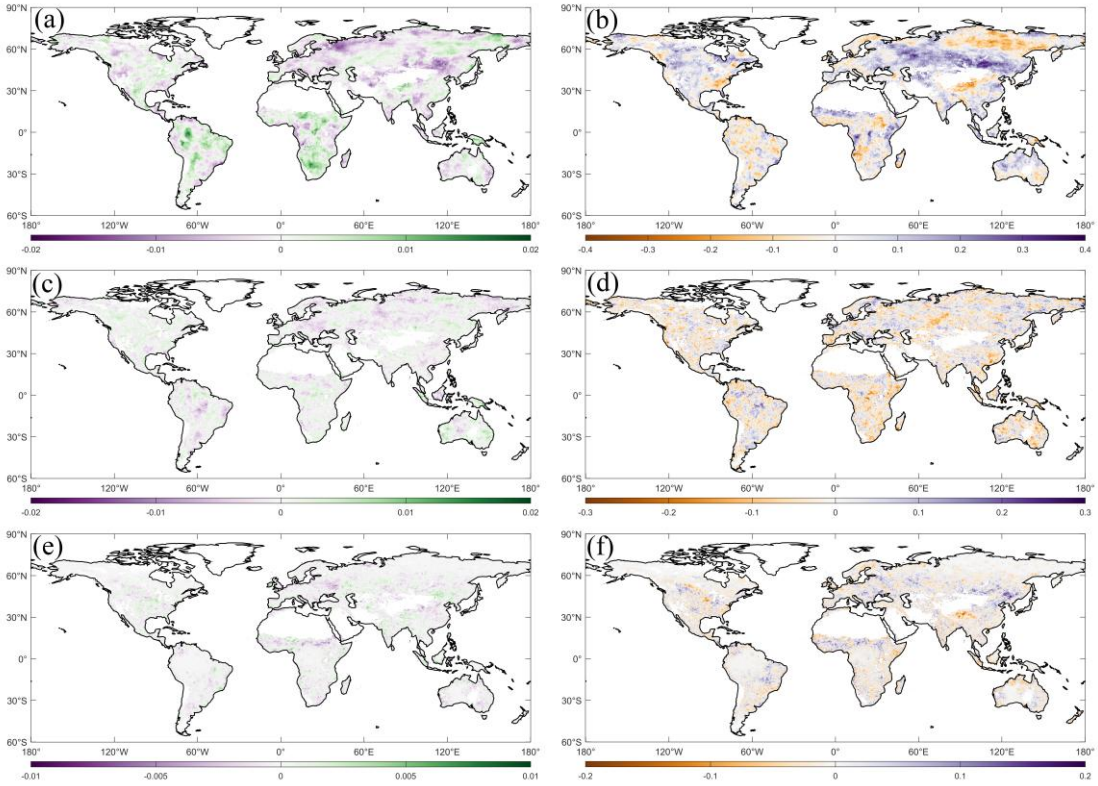

Figure S12. Variable contributions of CO_2, CLI, and LCC to R_{max} and T_{opt} under a 16-year moving window. (The left and right columns represent contributions to correlation coefficients and lag times, respectively, while the rows from top to bottom indicate the contributions of CO_2, CLI, and LCC.)

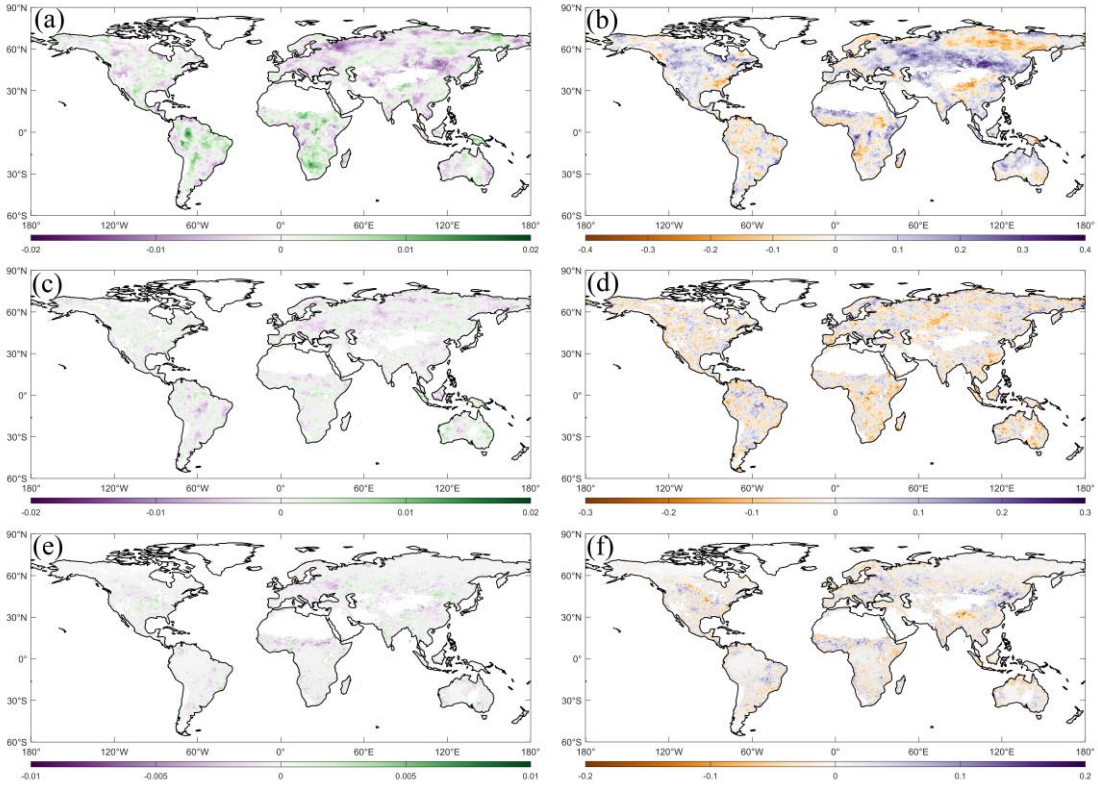

Figure S13. Variable contributions of CO_2, CLI, and LCC to R_{max} and T_{opt} under a 20-year moving window. (The left and right columns represent contributions to correlation coefficients and lag times, respectively, while the rows from top to bottom indicate the contributions of CO_2, CLI, and LCC.)

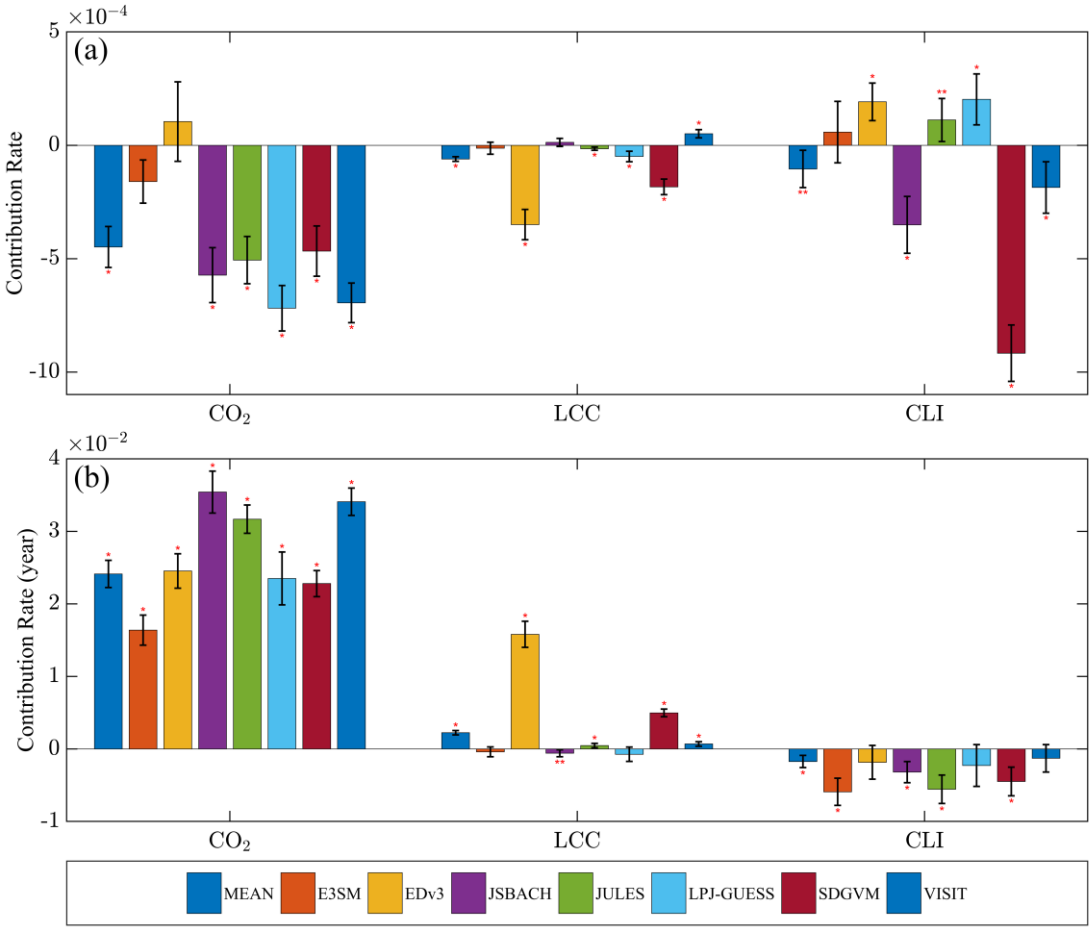

131

132 Figure S14. Variable contributions separated by TRENDY under a 16-year moving

133 window.

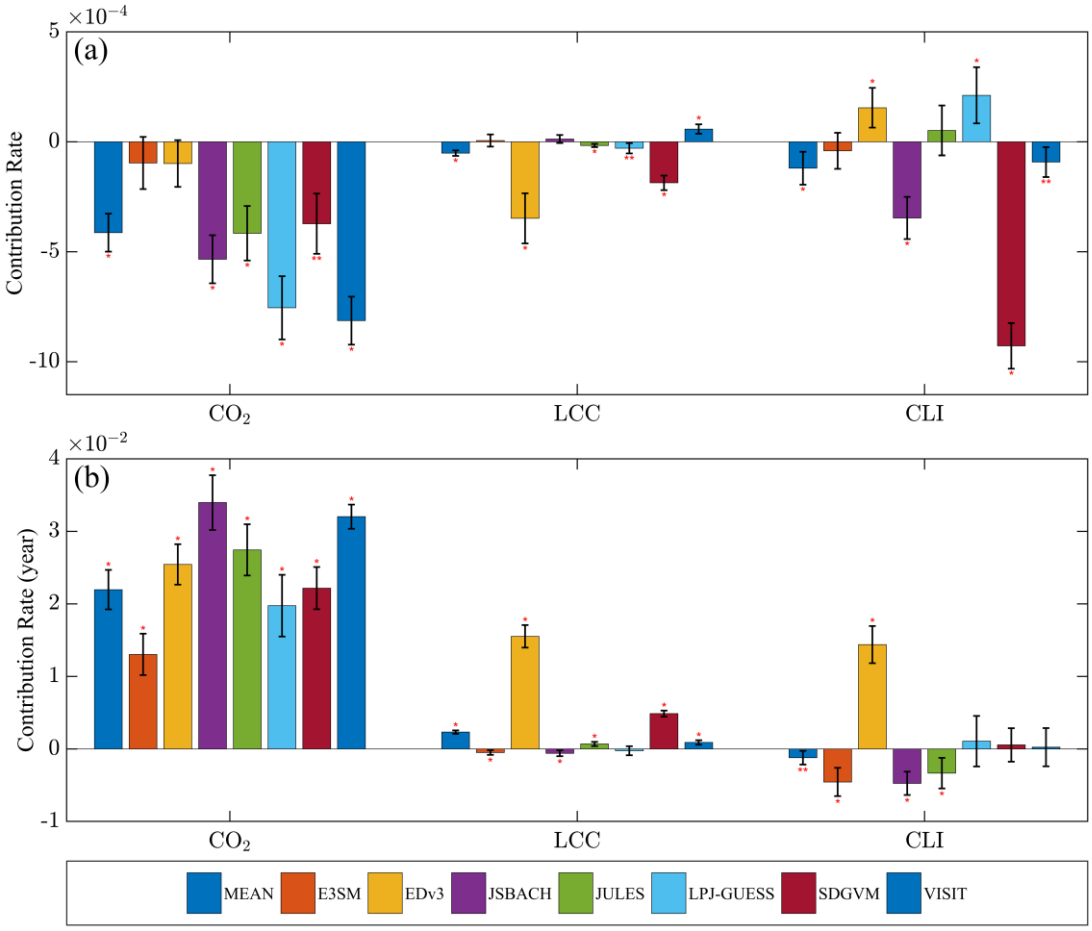

134

135 Figure S15. Variable contributions separated by TRENDY under a 20-year moving

136 window.

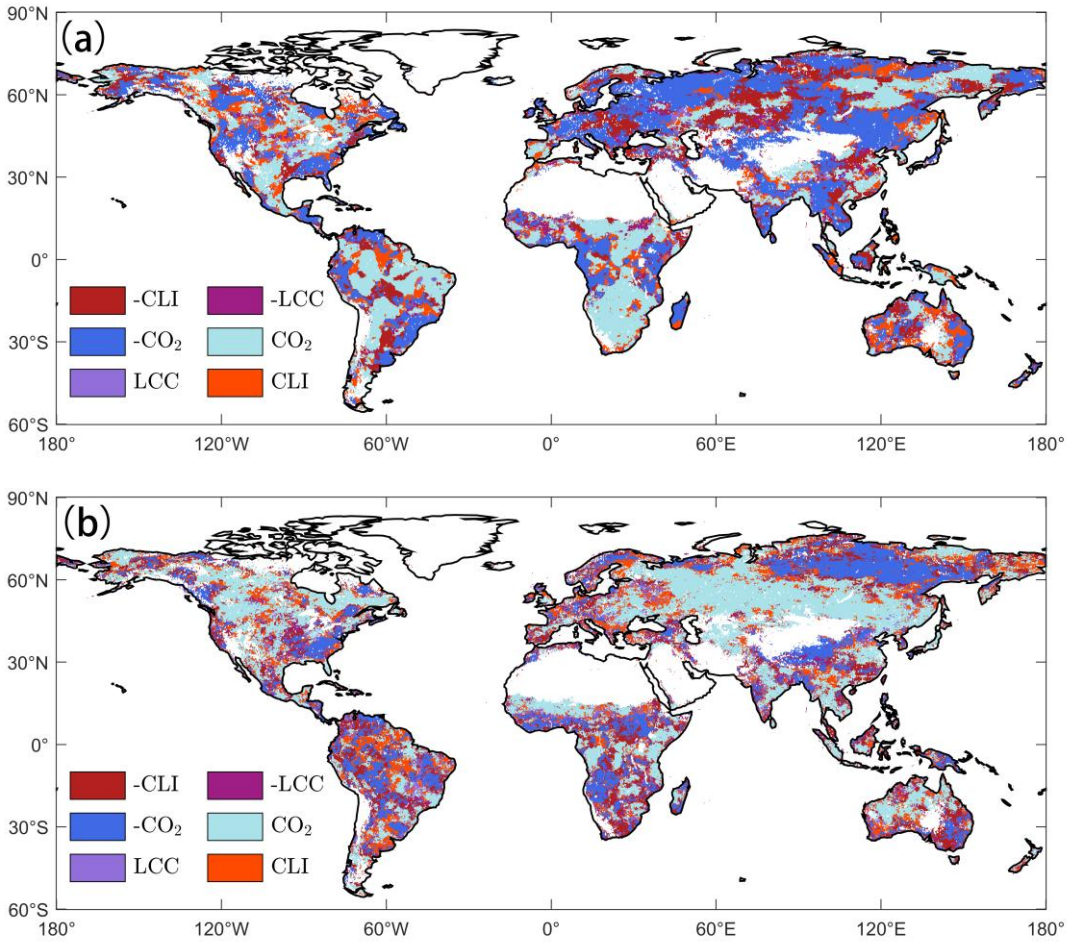

137

138 Figure S16. Spatial distribution of the dominant factors of CO_2, LCC, and CLI on (a)

139 the R_{max} and (b) T_{opt} under a 16-year moving window.

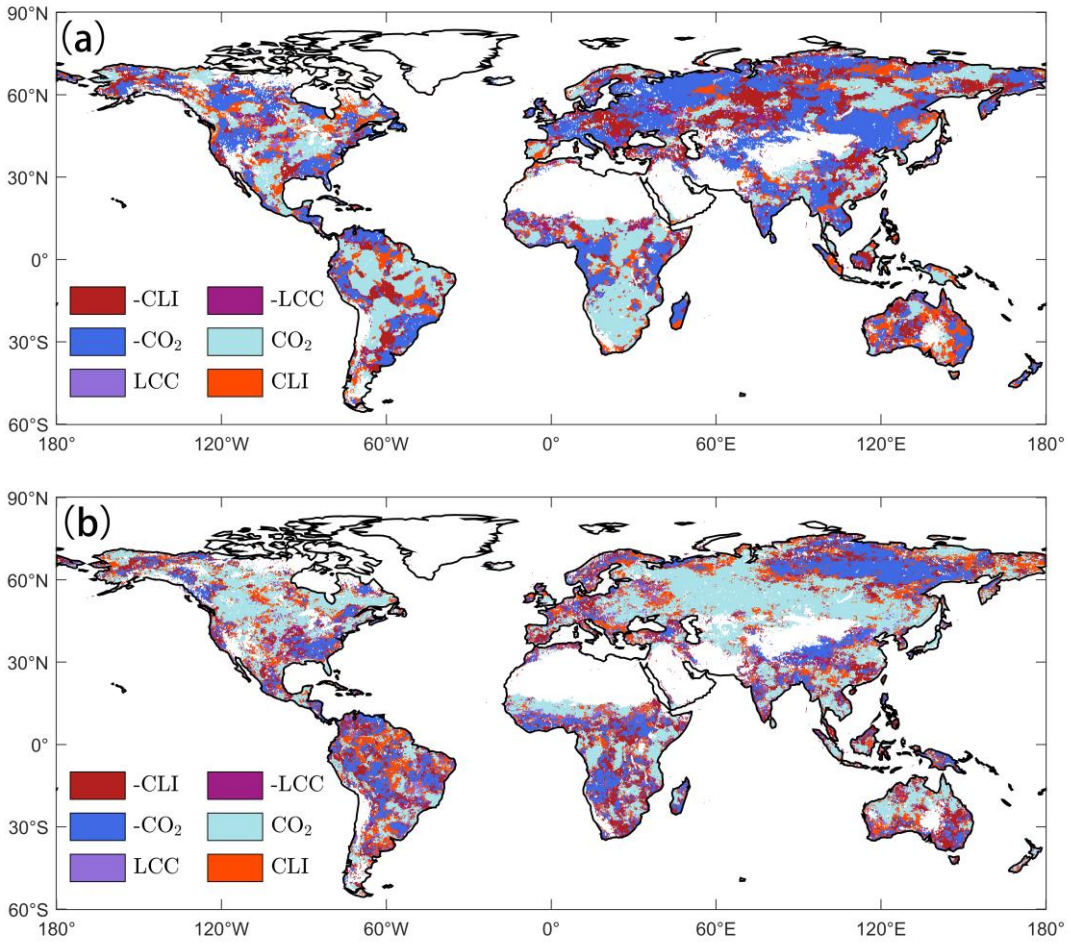

140

141 Figure S17. Spatial distribution of the dominant factors of CO_2, LCC, and CLI on (a)

142 the R_{max} and (b) T_{opt} under a 20-year moving window.

143

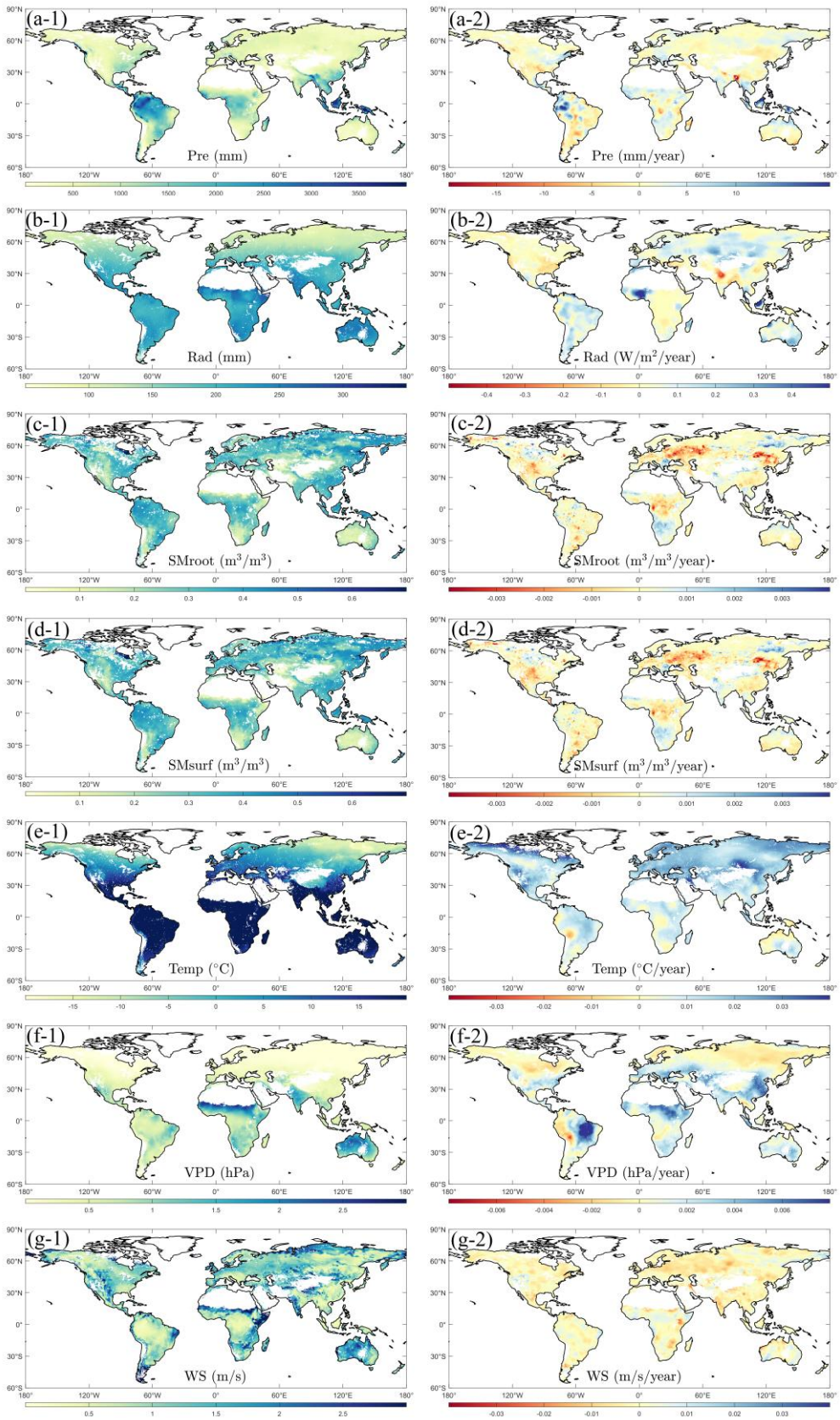

144

145 Figure S18. Spatial distribution of (1) mean and (2) change rates for (a) Pre, (b) Rad,

146 (c) SMroot, (d) SMsurf, (e) Temp, (f) VPD, and (g) WS.

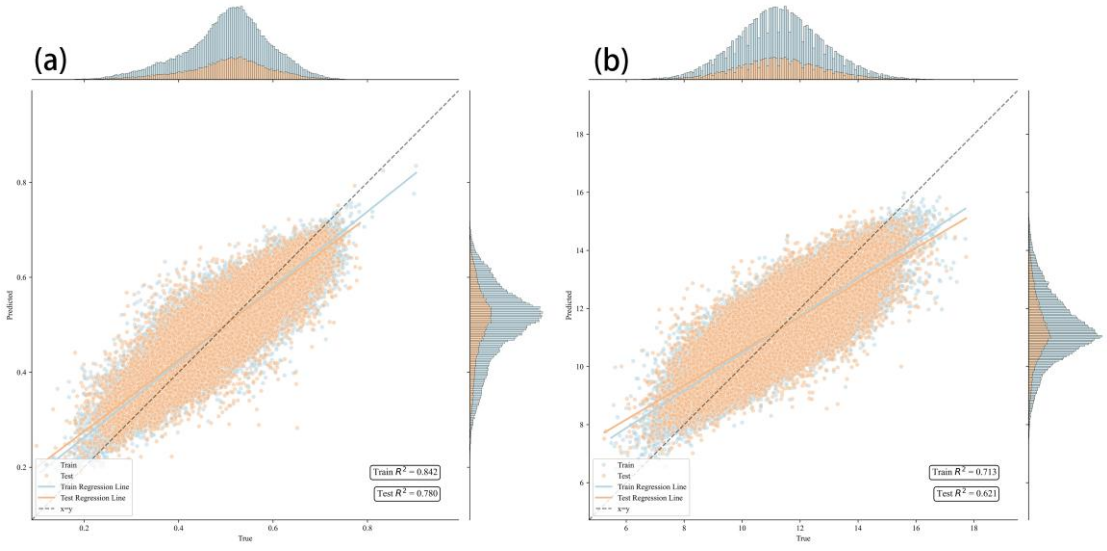

147

148 Figure S19. Model validation of (a) R_{max} and (b) T_{opt} based on XGBoost predictions.

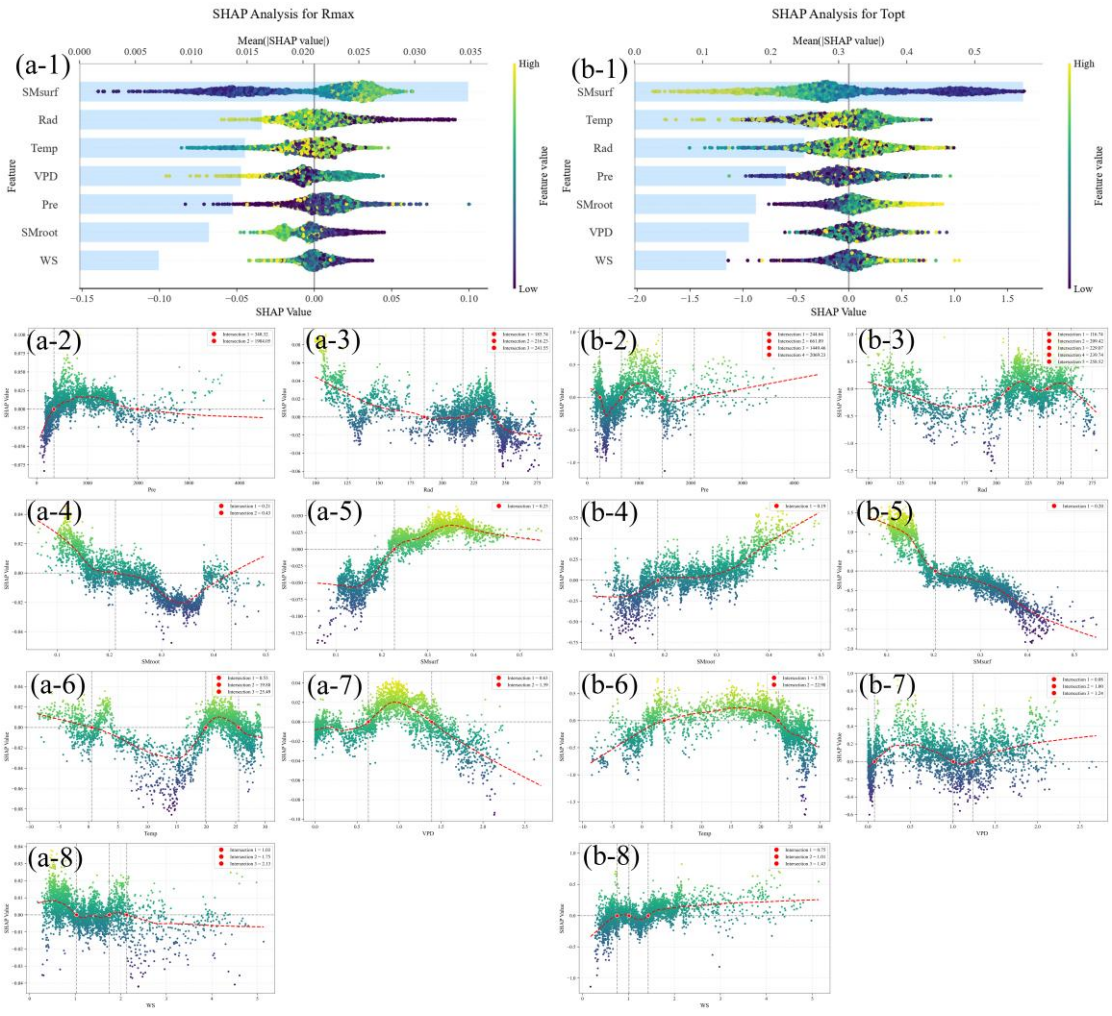

149

150 Figure S20. Global and local SHAP analyses of the effects of hydrothermal factors on

151 (a) R_{max} and (b) T_{opt} in Shrub. Panel 1 presents the global SHAP analysis, while panels

152 2–9 illustrate the local SHAP analyses for Pre, Rad, SMroot, SMsurf, Temp, VPD and

153 WS on R_{max} and T_{opt}, respectively.

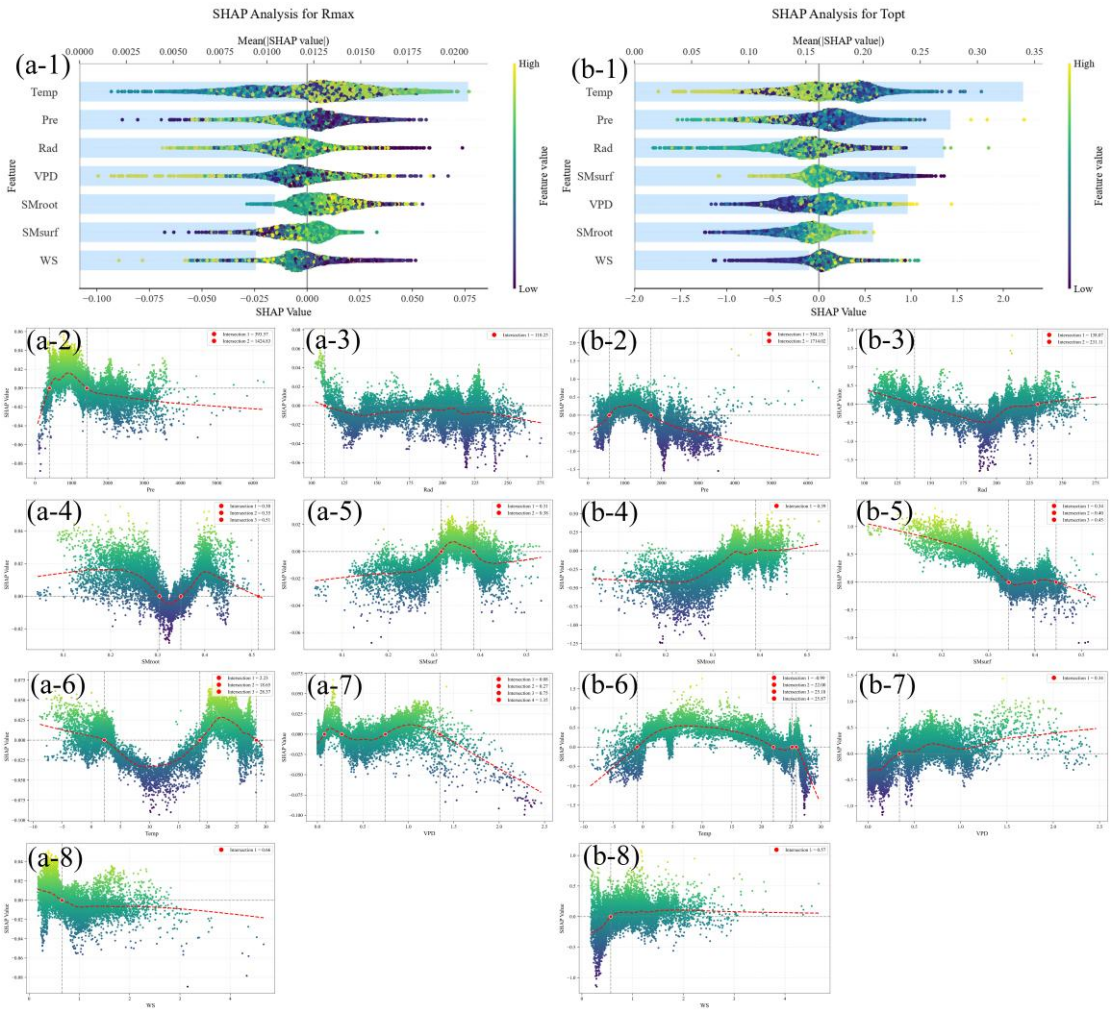

Figure S21. Global and local SHAP analyses of the effects of hydrothermal factors on (a) R_{max} and (b) T_{opt} in Forest. Panel 1 presents the global SHAP analysis, while panels 2–9 illustrate the local SHAP analyses for Pre, Rad, SMroot, SMsurf, Temp, VPD and WS on R_{max} and T_{opt}, respectively.

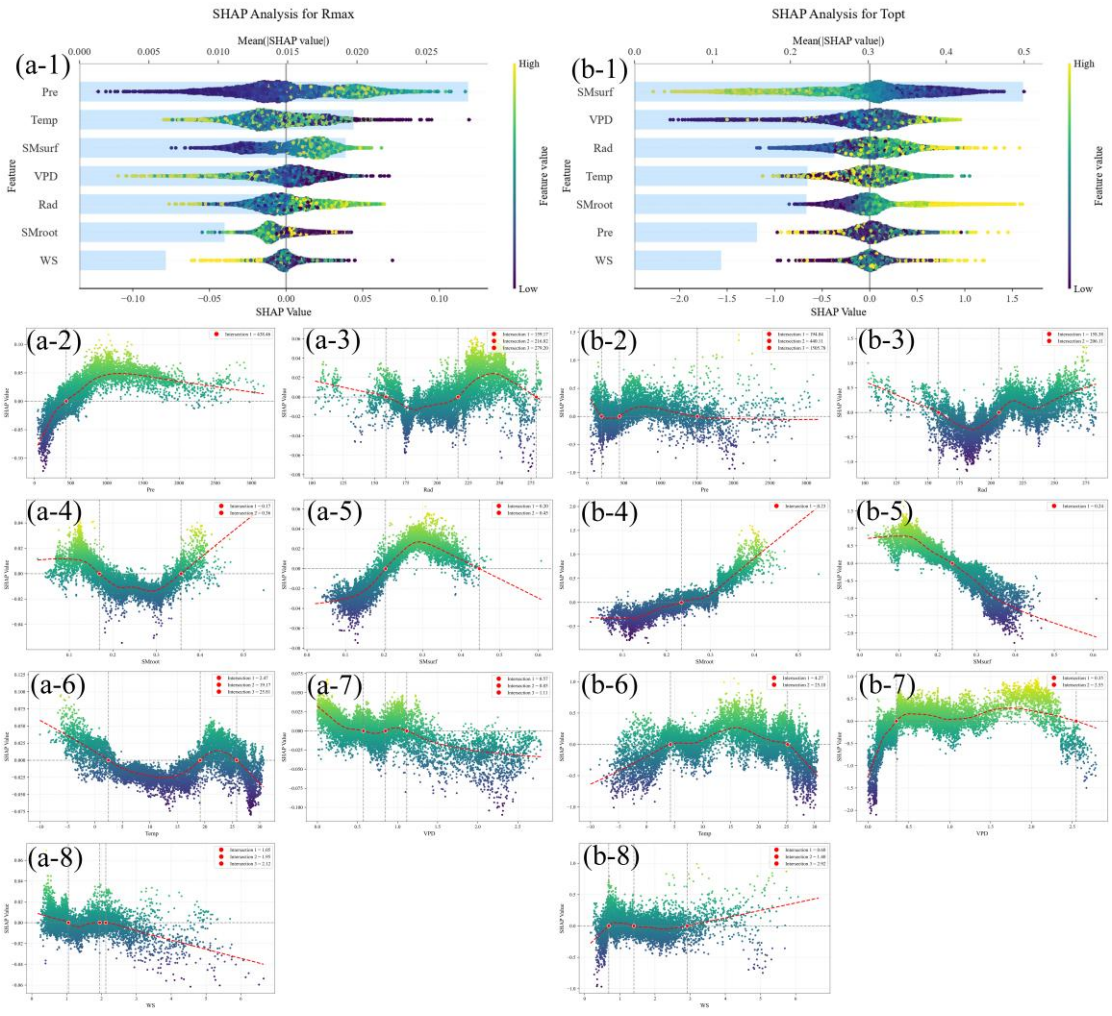

Figure S22. Global and local SHAP analyses of the effects of hydrothermal factors on (a) R_{max} and (b) T_{opt} in Pasture. Panel 1 presents the global SHAP analysis, while panels 2–9 illustrate the local SHAP analyses for Pre, Rad, SMroot, SMsurf, Temp, VPD and WS on R_{max} and T_{opt}, respectively.

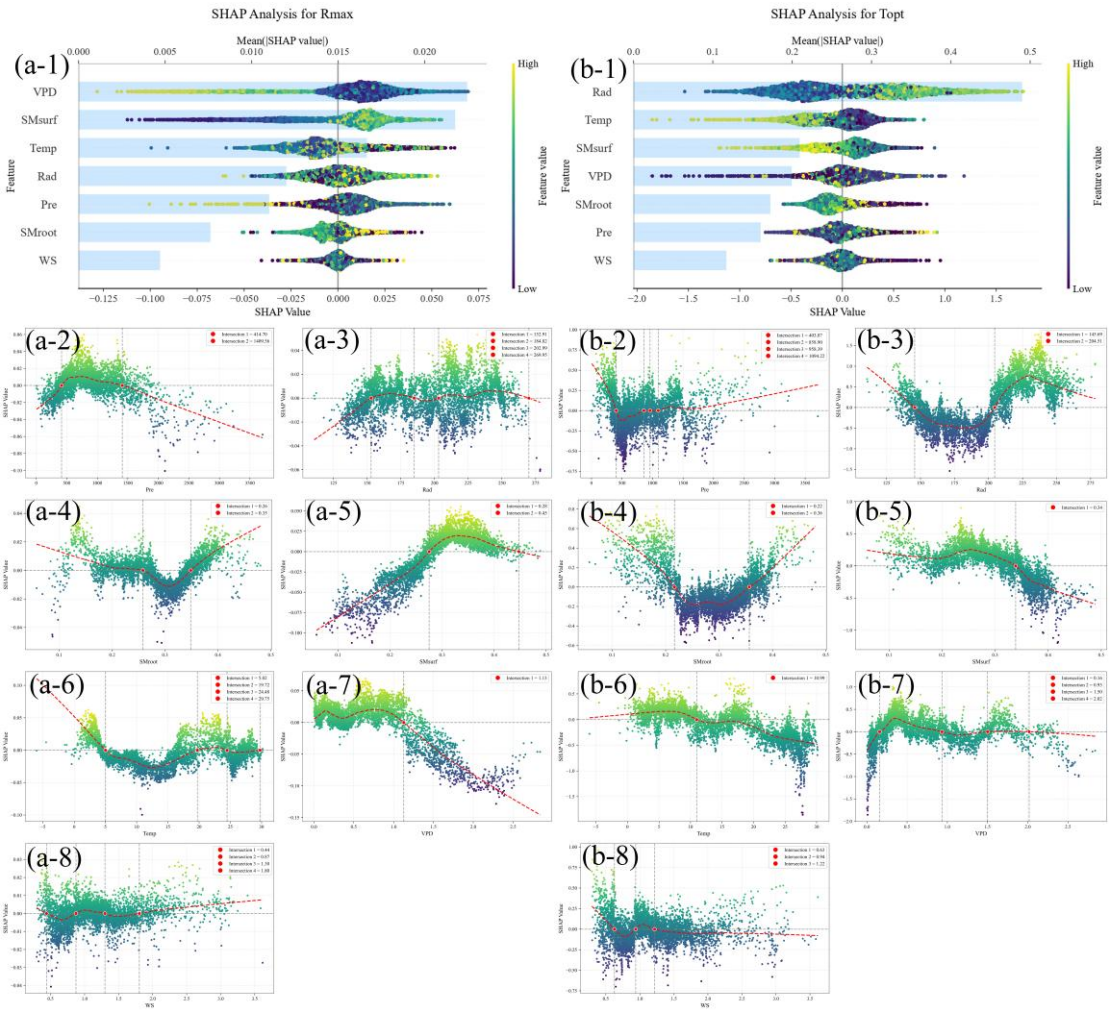

166

167 Figure S23. Global and local SHAP analyses of the effects of hydrothermal factors on

168 (a) R_{max} and (b) T_{opt} in Cropland. Panel 1 presents the global SHAP analysis, while

169 panels 2–9 illustrate the local SHAP analyses for Pre, Rad, SMroot, SMsurf, Temp,

170 VPD and WS on R_{max} and T_{opt}, respectively.

171

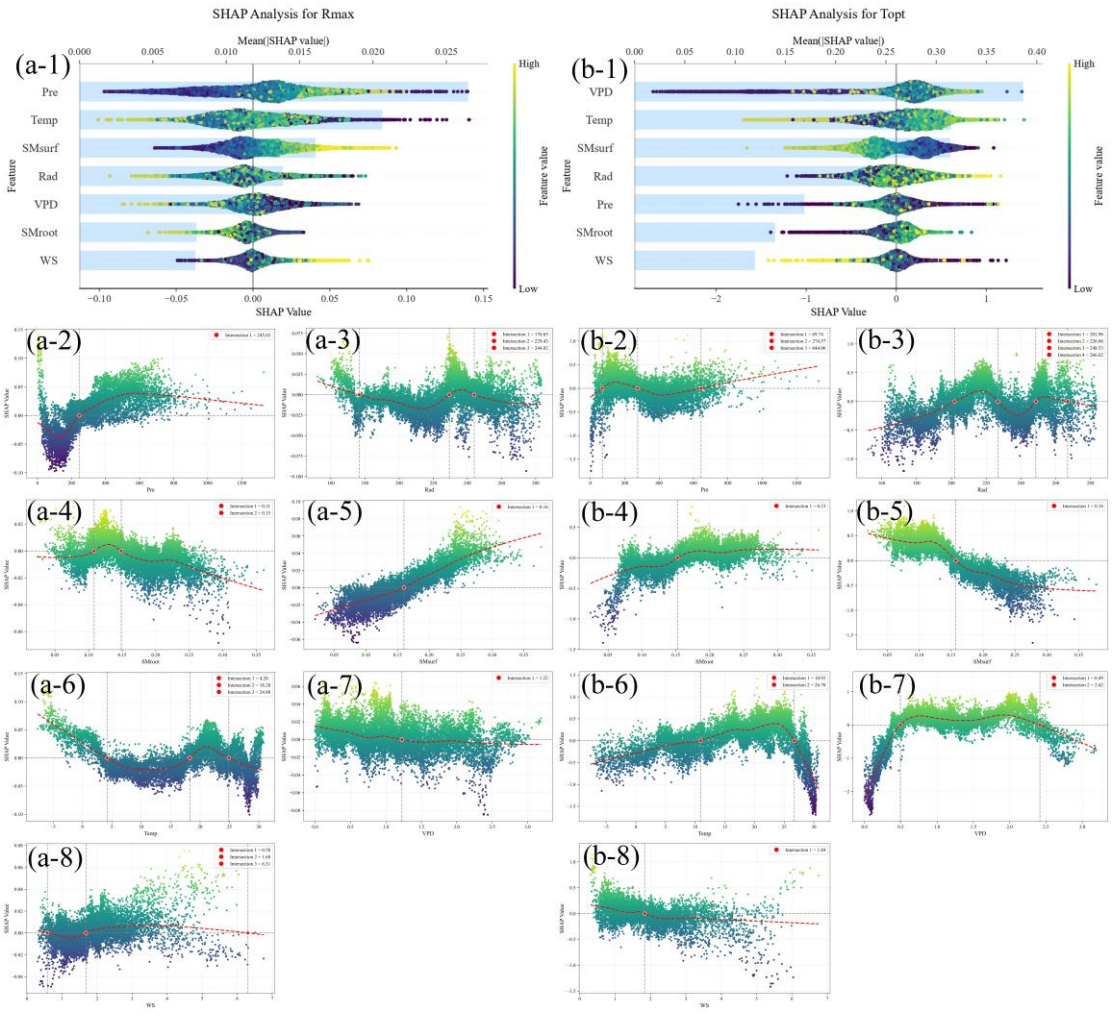

172

173 Figure S24. Global and local SHAP analyses of the effects of hydrothermal factors on

174 (a) R_{max} and (b) T_{opt} in AR. Panel 1 presents the global SHAP analysis, while panels

175 2–9 illustrate the local SHAP analyses for Pre, Rad, SMroot, SMsurf, Temp, VPD and

176 WS on R_{max} and T_{opt}, respectively.

177

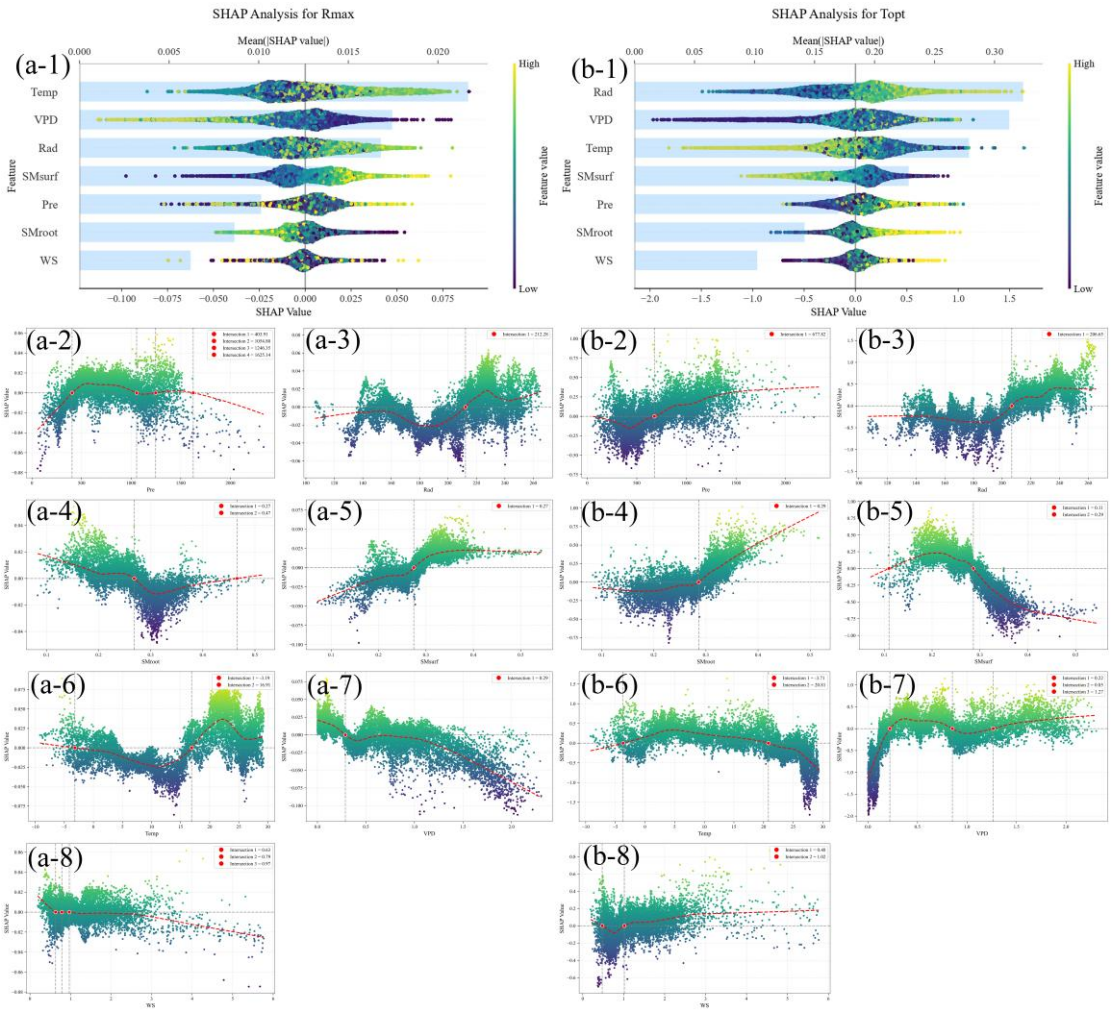

178

179 Figure S25. Global and local SHAP analyses of the effects of hydrothermal factors on

180 (a) R_{max} and (b) T_{opt} in SAR. Panel 1 presents the global SHAP analysis, while panels

181 2–9 illustrate the local SHAP analyses for Pre, Rad, SMroot, SMsurf, Temp, VPD and

182 WS on R_{max} and T_{opt}, respectively.

183

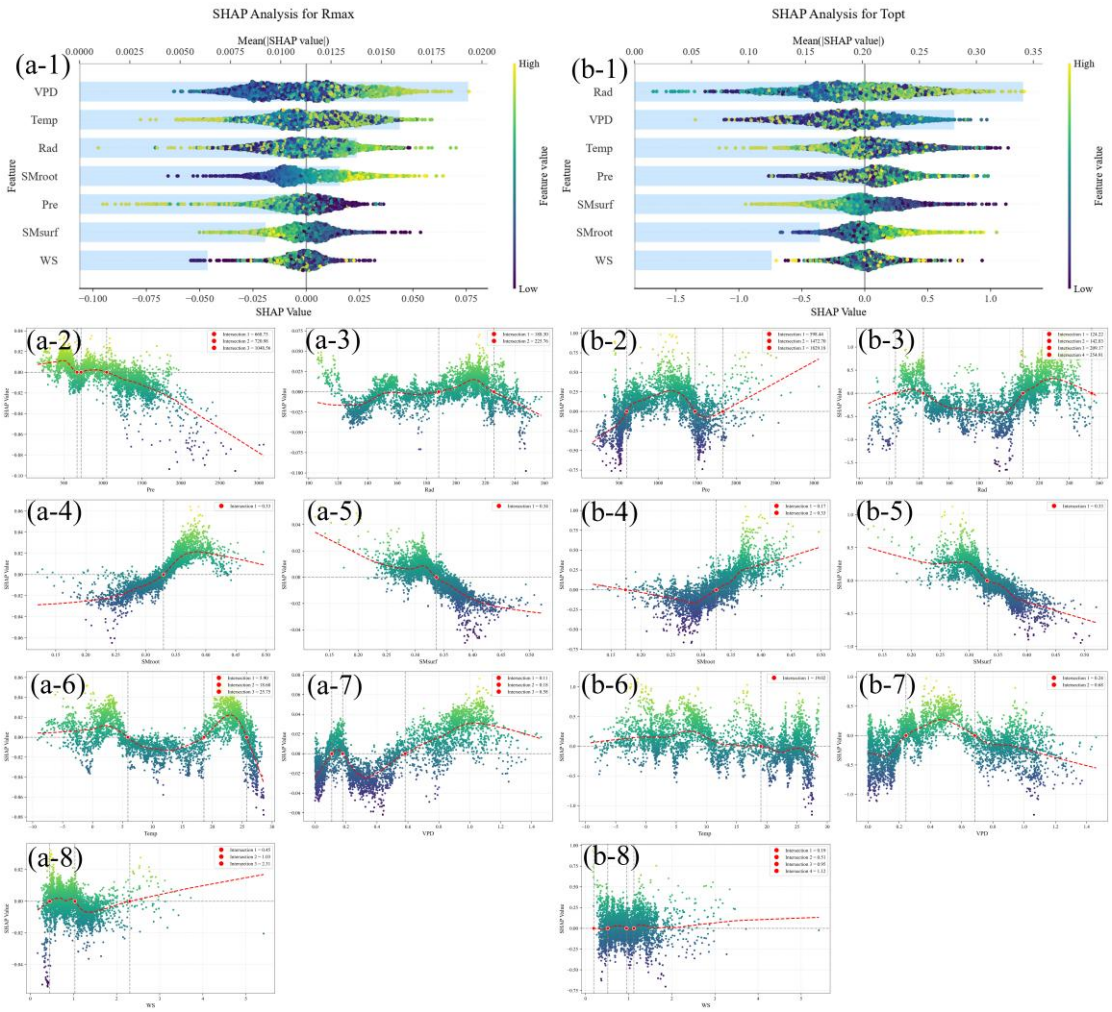

184

185 Figure S26. Global and local SHAP analyses of the effects of hydrothermal factors on

186 (a) R_{max} and (b) T_{opt} in SH. Panel 1 presents the global SHAP analysis, while panels

187 2–9 illustrate the local SHAP analyses for Pre, Rad, SMroot, SMsurf, Temp, VPD and

188 WS on R_{max} and T_{opt}, respectively.

189

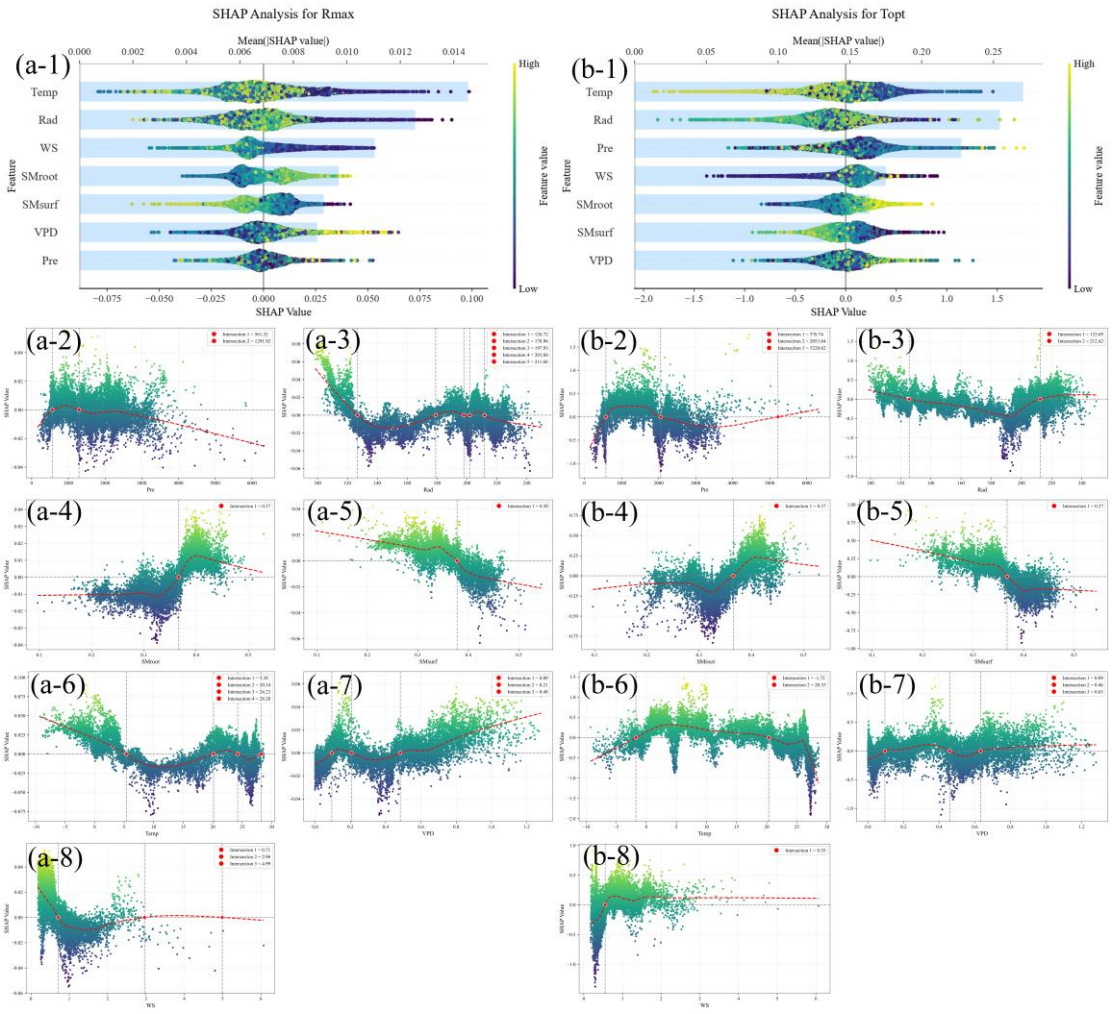

190

191 Figure S27. Global and local SHAP analyses of the effects of hydrothermal factors on

192 (a) R_{max} and (b) T_{opt} in HR. Panel 1 presents the global SHAP analysis, while panels

193 2–9 illustrate the local SHAP analyses for Pre, Rad, SMroot, SMsurf, Temp, VPD and

194 WS on R_{max} and T_{opt}, respectively.

195

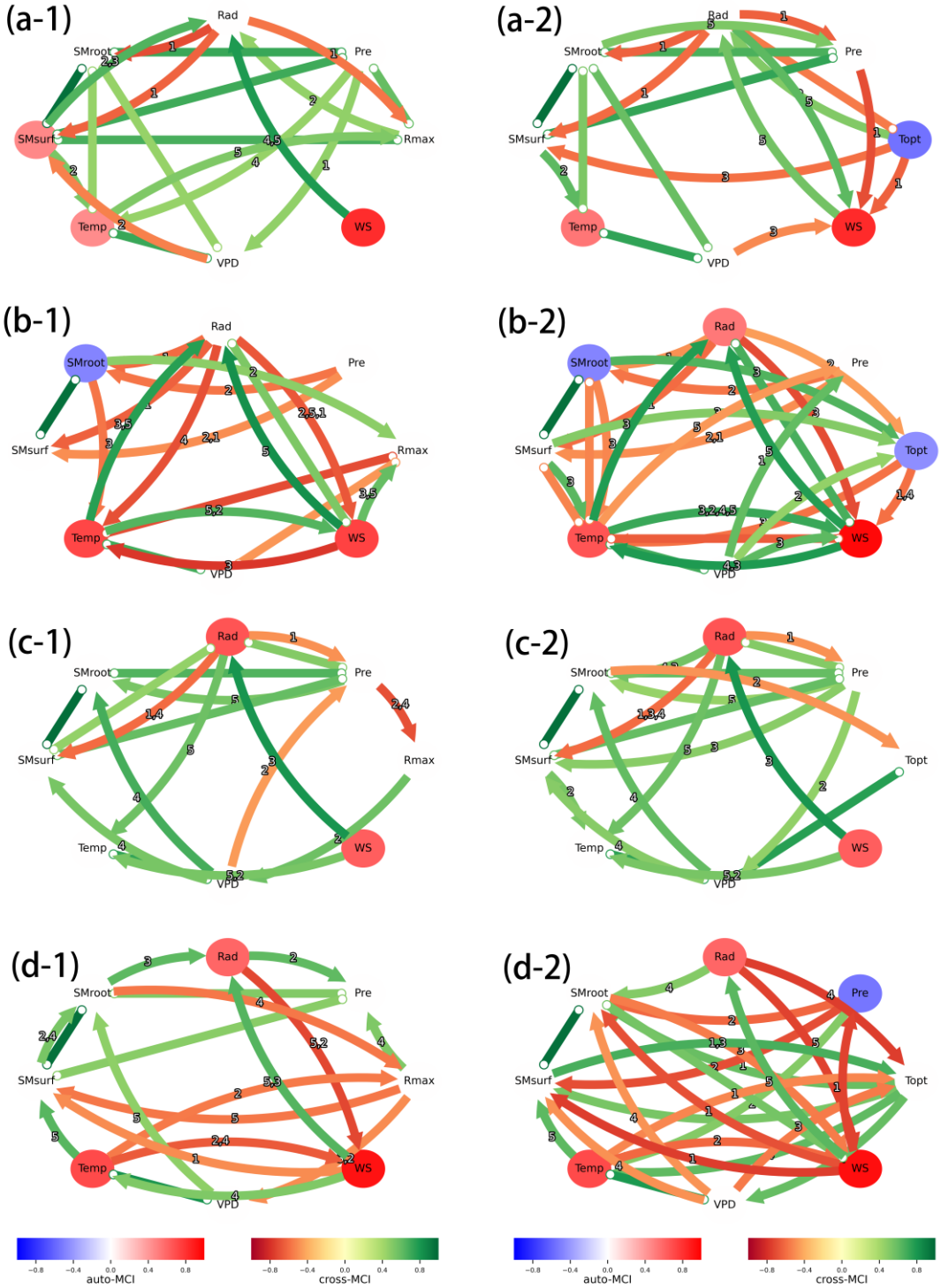

196

197 Figure S28. Causal network diagram of hydrothermal factors, R_{max}, and T_{opt} across

198 different vegetation types under AR.

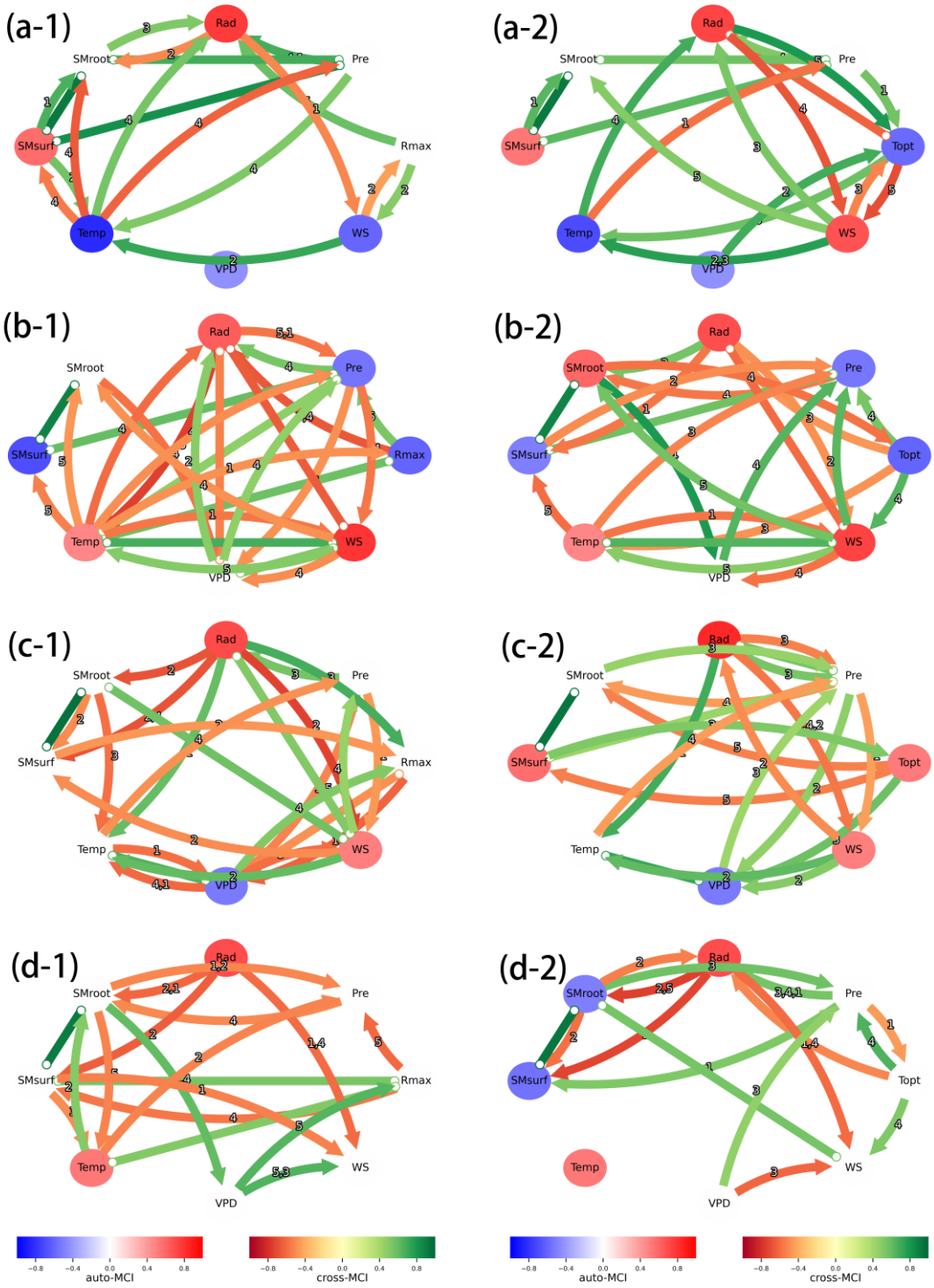

Figure S29. Causal network diagram of hydrothermal factors, R_{max}, and T_{opt} across different vegetation types under SAR.

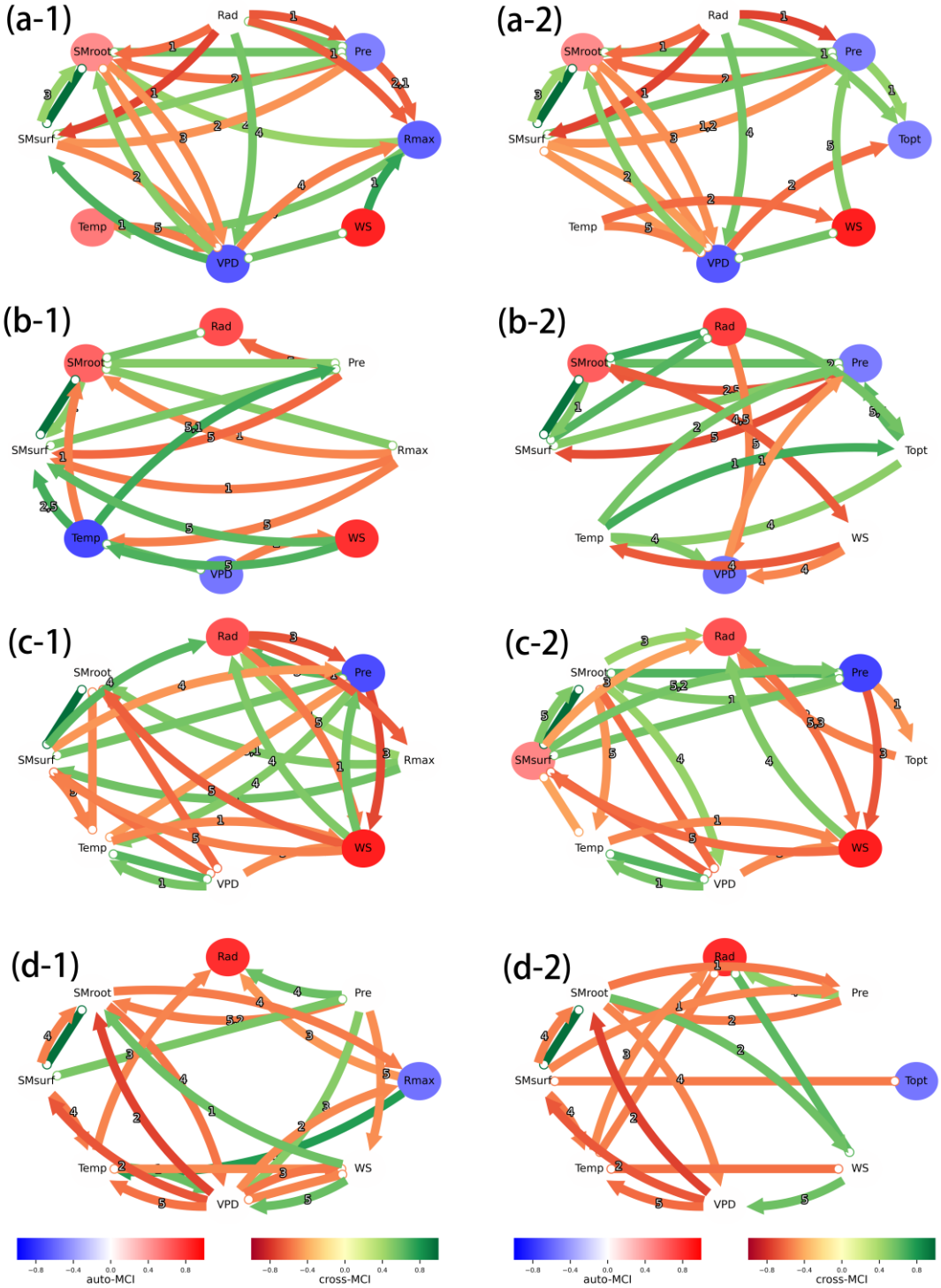

202

203 Figure S30. Causal network diagram of hydrothermal factors, R_{max}, and T_{opt} across

204 different vegetation types under SH.

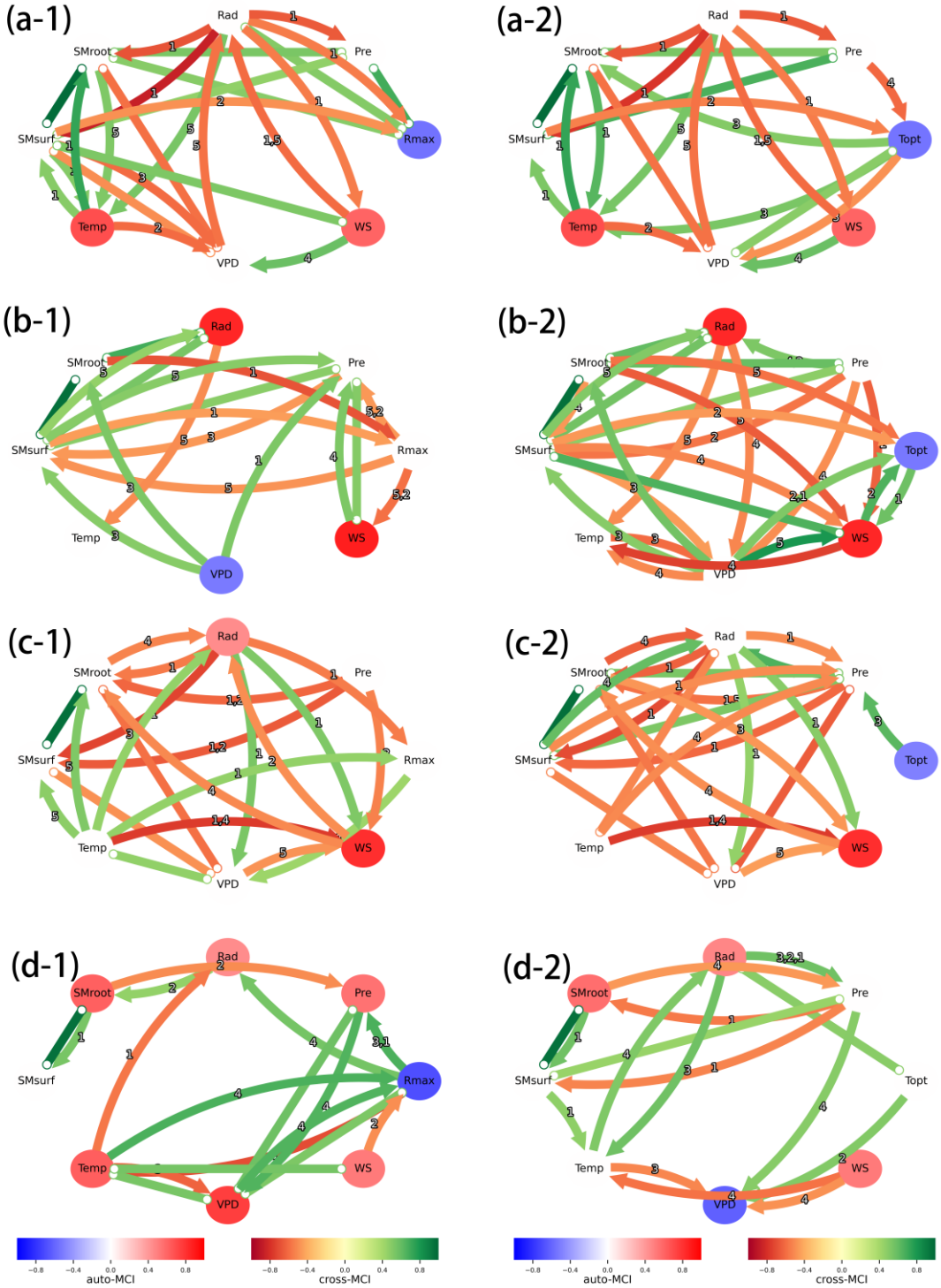

Figure S31. Causal network diagram of hydrothermal factors, R_{max}, and T_{opt} across different vegetation types under HR.

208 Table S1. Basic information of the 85 selected FLUXNET 2015 sites

SITE_ID	Lat	Lon	IGBP
AT-Neu	47.1167	11.3175	GRA
AU-ASM	-22.283	133.249	SAV
AU-Cpr	-34.0021	140.5891	SAV
AU-Cum	-33.6152	150.7236	EBF
AU-DaP	-14.0633	131.3181	GRA
AU-DaS	-14.1593	131.3881	SAV
AU-Dry	-15.2588	132.3706	SAV
AU-How	-12.4943	131.1523	WSA
AU-Stp	-17.1507	133.3502	GRA
AU-Tum	-35.6566	148.1517	EBF
AU-Wom	-37.4222	144.0944	EBF
BE-Lon	50.5516	4.7462	CRO
BR-Sa1	-2.8567	-54.9589	EBF
CA-Gro	48.2167	-82.1556	MF
CA-NS2	55.9058	-98.5247	ENF
CA-NS3	55.9117	-98.3822	ENF
CA-NS5	55.8631	-98.485	ENF
CA-NS6	55.9167	-98.9644	OSH
CA-Obs	53.9872	-105.118	ENF
CA-Qfo	49.6925	-74.3421	ENF
CA-SF2	54.2539	-105.878	ENF
CA-SF3	54.0916	-106.005	OSH
CA-TP1	42.6609	-80.5595	ENF
CA-TP2	42.7744	-80.4588	ENF
CA-TP3	42.7068	-80.3483	ENF
CA-TP4	42.7102	-80.3574	ENF
CH-Cha	47.2102	8.4104	GRA
CH-Dav	46.8153	9.8559	ENF
CH-Fru	47.1158	8.5378	GRA
CH-Lae	47.4783	8.3644	MF
CH-Oe1	47.2858	7.7319	GRA
CH-Oe2	47.2864	7.7337	CRO
CZ-BK1	49.5021	18.5369	ENF
CZ-BK2	49.4944	18.5429	GRA
CZ-wet	49.0247	14.7704	WET
DE-Akm	53.8662	13.6834	WET
DE-Geb	51.0997	10.9146	CRO
DE-Gri	50.95	13.5126	GRA
DE-Hai	51.0792	10.4522	DBF
DE-Kli	50.8931	13.5224	CRO
DE-Lkb	49.0996	13.3047	ENF
DE-Lnf	51.3282	10.3678	DBF
DE-Obe	50.7867	13.7213	ENF

DE-Spw	51.8922	14.0337	WET
ES-Amo	36.8336	-2.2523	OSH
ES-LJu	36.9266	-2.7521	OSH
FR-Fon	48.4764	2.7801	DBF
FR-Gri	48.8442	1.9519	CRO
FR-LBr	44.7171	-0.7693	ENF
GF-Guy	5.2788	-52.9249	EBF
IT-BCi	40.5237	14.9574	CRO
IT-Cpz	41.7052	12.3761	EBF
IT-Lav	45.9562	11.2813	ENF
IT-MBo	46.0147	11.0458	GRA
IT-Noe	40.6062	8.1517	CSH
IT-Ro1	42.4081	11.93	DBF
IT-Ro2	42.3903	11.9209	DBF
IT-Tor	45.8444	7.5781	GRA
JP-SMF	35.2617	137.0788	MF
MY-PSO	2.973	102.3062	EBF
NL-Hor	52.2403	5.0713	GRA
US-ARM	36.6058	-97.4888	CRO
US-Blo	38.8953	-120.633	ENF
US-Cop	38.09	-109.39	GRA
US-GLE	41.3665	-106.24	ENF
US-Goo	34.2547	-89.8735	GRA
US-IB2	41.8406	-88.241	GRA
US-Los	46.0827	-89.9792	WET
US-Me2	44.4526	-121.559	ENF
US-Me3	44.3154	-121.608	ENF
US-Me6	44.3233	-121.608	ENF
US-Ne1	41.1651	-96.4766	CRO
US-Ne2	41.1649	-96.4701	CRO
US-Ne3	41.1797	-96.4397	CRO
US-Oho	41.5545	-83.8438	DBF
US-SRC	31.9083	-110.84	OSH
US-SRG	31.7894	-110.828	GRA
US-Sta	41.3966	-106.802	OSH
US-Syv	46.242	-89.3477	MF
US-Twt	38.1087	-121.653	CRO
US-UMB	45.5598	-84.7138	DBF
US-UMd	45.5625	-84.6975	DBF
US-WCr	45.8059	-90.0799	DBF
US-Whs	31.7438	-110.052	OSH
US-Wkg	31.7365	-109.942	GRA